Exposed H_2O-rich areas detected on Ceres with the Dawn Visible and InfraRed mapping spectrometer

Jean-Philippe Combe[1*], Andrea Raponi[2], Federico Tosi[2], Maria Cristina De Sanctis[2], Filippo Giacomo Carrozzo[2], Francesca Zambon[2], Eleonora Ammannito[2,3,4], Kynan H.G. Hughson[4], Andreas Nathues[5], Martin Hoffmann[5], Thomas Platz[5,6], Guneshwar Thangjam[5], Norbert Schorghofer[6], Stefan Schröder[7], Shane Byrne[8], Margaret E. Landis[8], Ottaviano Ruesch[9], Thomas B. McCord[1], Katherine E. Johnson[1], Sandeep Magar Singh[1], Carol A. Raymond[10], Christopher T. Russell[4]

[1]Bear Fight Institute, 22 Fiddler's Road, P.O. Box 667, Winthrop, WA 98862, USA.
[2]Istituto di Astrofisica e Planetologia Spaziali-Istituto Nazionale di Astrofisica, Rome, Italy.
[3]Agenzia Spaziale Italiana, Rome, Italy.
[4]Institute of Geophysics and Planetary Physics, University of California Los Angeles, CA, USA.
[5]Max Planck Institute for Solar System Research, Planets and Comets Department, 37077 Göttingen, Germany.
[6]Planetary Science Institute, Tucson, AZ, USA.
[7]Deutsches Zentrum für Luft- und Raumfahrt, Department German Aerospace Center Institute of Planetary Research. Planetary Geology Rutherfordstraße 2, 12489 Berlin, Germany.
[8]Lunar and Planetary Laboratory, Tucson, AZ, USA.
[9]European Space Agency, European Space Research and Technology Centre, Noordwijk, The Netherlands.
[10]Jet Propulsion Laboratory, Pasadena, CA, USA.

*Correspondence to: jean-philippe_combe@bearfightinstitute.com / Fax: +001-509-996-3772.

Submitted to Icarus

Contents

Abstract

H_2O-rich materials are locally exposed at the surface of Ceres as discovered from infrared reflectance spectra of the Visible and InfraRed mapping spectrometer (VIR) of the Dawn mission. Nine locations on Ceres exhibit diagnostic absorption bands of the H_2O molecule at 2.00, 1.65 and 1.28 μm. The detections are all consistent with H_2O ice mixed with low-albedo components. All the reported H_2O exposures occur at latitudes poleward of 30° in fresh craters near rim shadows, have a surface area < 7 km^2, and are associated with one or more surface features such as a morphological flow or landslide, fractures, high albedo, or a pole-facing slope (one case is confirmed to be adjacent to persistent shadow). In four occurrences, these detections are associated with small (<0.1 km^2) high-albedo areas that can be recognized in high-resolution imagery (~35 m/pixel) from the Framing Camera (FC). Since all these observations are compatible with an H_2O-rich subsurface, the replenishment of surficial H_2O likely comes from the ice that is present underneath. In four other occurrences, H_2O is detected on walls and floors of fresh impact craters, either in the shadow or adjacent to shadows, which suggests that local thermodynamical conditions may also favor the concentration of H_2O in these areas.

Highlights

- Exposed H_2O-rich materials at Ceres' surface have been detected in VIR spectra at 9 different locations.
- H_2O ice is the component that most likely explains the H_2O detections in the spectra.
- All H_2O absorption features are detected at latitudes above 30° and over areas of a few km^2 at most.
- Exposed ice is rare, even though subsurface ice is ubiquitous.

Keywords

- Dwarf planet Ceres
- Surface composition
- Exposed H_2O ice
- Reflectance spectroscopy

1. Introduction

H_2O is a fundamental component of Ceres, as inferred from almost four decades of ground telescopic observations, geophysical modeling, and two years in orbit by the Dawn mission. To date, surficial H_2O on Ceres has been detected by Dawn's Visible and InfraRed mapping spectrometer (VIR) in three fresh impact craters such as Oxo (Combe et al., 2016), a small, unnamed crater at 70°N (Platz et al., 2016; Ermakov et al.,2017), and Juling Crater (Raponi et al., 2017). Further potential ice-rich depositions in permanently shadowed craters have been identified (Platz et al., 2016). In addition, the surface morphology observed at high resolution in images from Dawn's Framing Camera (FC) revealed possible cryovolcanism (Ruesch et al., 2016; Nathues et al., 2017) and flow-like morphological features that could be due to ground H_2O ice (Schmidt et al., 2017). The presence of significant amounts of H_2O is further supported by the inferred upper crust stratigraphy of Ceres (Nathues et al., 2016). From Dawn's Gamma-Ray and Neutron Detector (GRaND), hydrogen was detected within 1 meter of the subsurface (between 16 and 29 weight % in H_2O-equivalent H), and its distribution is interpreted as a variation of the ice table depth as a function of latitude (Prettyman et al., 2016). Before the Dawn mission, H_2O was inferred to be a likely component from calculation of its mass, size and low bulk density (McCord and Sotin, 2005), its shape that suggested differentiation (Thomas et al., 1997) and from thermophysical modeling. Thermodynamical models of its internal structure indicated differentiation with amounts of H_2O as high as 26% in the average bulk composition (McCord and Sotin, 2005; Castillo-Rogez and McCord, 2010) and 48-55% in the 70-190 km of its crust (Park et al., 2016). The importance of H_2O in the chemistry of Ceres came from spectral properties in the near-infrared that revealed hydroxylated minerals likely resulting from the aqueous alteration of silicate rocks by water (Lebofsky et al., 1981; Vernazza et al., 2005; Rivkin et al., 2006; Milliken and Rivkin, 2009; De Sanctis et al., 2015; Ammannito et al., 2016). Evidence of transient phenomena was also reported, such as OH florescence over the north pole (A'Hearn et al., 1992), the release of H_2O molecules (Küppers et al., 2014), the presence of haze above high-albedo facula€ (Nathues et al., 2015; Thangjam et al., 2016), and the temporary acceleration of the solar wind around Ceres that could be explained by a temporary exosphere (Villareal et al., 2017), although none has reported temporal variations at the surface due to the suggested activity. All of these studies are consistent with the fundamental role of H_2O in the evolution and internal activity of Ceres over geological times that may have led to partial differentiation, the release of H_2O similar to cometary activity, and the cause of possible transient phenomena at the surface in present times.

In this study, we present nine areas where H_2O-rich materials are exposed at the surface of Ceres, resulting from processing the entire VIR IR dataset of the Dawn mission at Ceres from the Approach phase to the end of the Low-Altitude Mapping Orbit phase. Our objective is to determine whether the surficial H_2O on Ceres is the expression of internal activity, or if it results from thermo-physical or mechanical processes of the surface. Meteoroid impacts, landslides, migration of H_2O molecules (Schorghofer et al., 2016), and cryovolcanism (Ruesch et al., 2016; Nathues et al., 2017) exist on Ceres and make the detection of H_2O possible today. Mechanical processes likely occur, as inferred from the discovery of H_2O in the Oxo crater (Combe et al., 2016), which suggests that a recent meteorite impact (less than 10 Ma) and very recent landslides have exposed H_2O from a water-ice rich subsurface (Nathues et al., 2017). The local pole-facing, 20° slope and the proximity of a sharp scarp that casts shadows likely favors the preservation of H_2O ice (Landis et al., 2017). By making an exhaustive inventory of H_2O-rich materials exposed on Ceres, we can gain insight into the distribution, extent, abundance, geological context and thermal conditions of these areas,

because the distribution of findings (local or widespread) can be indicative of the origin of surficial H_2O.

Reflectance spectroscopy is the only direct way to identify H_2O exposed at the surface of Ceres with the Dawn mission. As a consequence, a refined analysis of VIR spectra is suited for the finding of more H_2O-rich areas on Ceres. Examination of the morphological and albedo features with high-resolution imagery can help validate and interpret the geological context of any new detection. The methodology of spectral analysis of VIR IR spectra can be adapted to search for weak absorption bands of H_2O in individual spectra spread over a large dataset (several million spectra) in order to optimize the probability of detection. One technique – linear spectral unmixing – is easily reproducible, is fast enough to be manageable for large datasets, and can be fine-tuned for enhanced sensitivity to one or more absorption bands. The processing of remote-sensing spectra implies the selection of one or more reference spectra (spectral endmembers) that is associated with a known composition. The model finds the linear combination that results in the best fit, and it provides both weighing factors (mixing coefficient) and quality of fit (such as the Root-Mean Squares). Although this technique is primarily designed for the analysis of mixed components, it can also serve the function of spectral feature fitting for the search of specific absorption bands.

In the present study, we search for H_2O-rich materials in multiple areas on Ceres and study its distribution. VIR IR data were processed and analyzed specifically for the search of spectra similar to those of H_2O. All spectra associated to the nine findings of H_2O are consistent with the presence of ice. All areas of exposed H_2O-rich materials are located at latitudes above 30°, seven of them in the northern hemisphere, and two in the southern hemisphere. All H_2O detections are associated with surface albedo properties or morphological features as expected when H_2O is present in the surface material. Specifically, we identified four types of regions, based on the type of albedo or morphological properties.

2. Dawn VIR infrared data and processing methodology

2.1 Instrument and data specifications

For the detection and characterization of H_2O-rich areas on Ceres, we focused on the analysis of spectra from the infrared detector of Dawn's VIR imaging spectrometer (De Sanctis et al., 2011), which is sensitive to the radiation range 1.02–5.10 μm where vibration absorption processes of the H_2O molecule occur. VIR-IR is a push-broom detector constituted of 256 spatial pixels by 432 spectral pixels, with spectral sampling of 9.8 nm, and with an Instantaneous field of View (IFOV) of 250 μrad/pixel.

Dawn began observing Ceres in January 2015. The mission was divided into seven main observational phases (Table 1). Each phase differs in duration, illumination conditions (with the phase angle increasing from Survey to Low-Altitude Mapping Orbit (LAMO), and surface coverage. Global mapping was achieved by VIR for all latitudes below 70°, with some redundancy; only the polar regions were not observed. We used all VIR IR data available from the beginning of the Dawn mission at Ceres to August 26, 2016, which represents ~28.15×10^6 spectra in 1772 observation files.

Table 1: Dawn at Ceres mission phases.

Orbit phase	Dates	Altitude (km)	Resolution of FC (m/pixel)	Resolution of VIR (km/pixel)
Approach	December 1, 2014 – April 23, 2015	1.2e6-2.2e4	1.12e5 – 2.1e3	

RC3	April 23, 2015 – May 9, 2015	13500	1300	~ 3.64
Transfer to Survey				3.64 – 1.1
Survey	June 6, 2015 – June 30, 2015	4400	410	~ 1.1
High-Altitude Mapping Orbit (HAMO)	August 17, 2015 – October 23, 2015	1450	140	~ 0.36 -0.40
Low-Altitude Mapping Orbit (LAMO)	December 16, 2015 – September 2, 2016	375	35	~ 0.09 - 0.1
Extended Juling Orbit (CXJ)	October 5, 2016 – November 4, 2016	1450	140	~ 0.36 - 0.40

2.2 Calibration improvement

VIR IR level 1b data are already calibrated into radiance ($W.m^{-2}.sr^{-1}.\mu m^{-1}$), however they are still affected by instrument artifacts such as spikes (usually caused by cosmic rays), a saw-tooth effect in the spectra due to different gains of odd and even wavelength channels, systematic features in the spectra, and systematic vertical stripes in the images before geographical projection. All of these undesired effects can be minimized using threshold values for spike detection, median calculation for spike removal, flat field correction for minimization of systematic spatial artifacts; correction of the instrument responsivity function, and odd-even channel correction based on averaging. All of these calibration steps are described in detail in Combe et al. (2015), except for two of them that are now performed differently: 1) the flat-field correction now relies on the analysis of the entire Vesta and Ceres VIR IR dataset instead of just the Vesta observations, and 2) the instrument responsivity function is adjusted to ground observations (Carrozzo et al., 2016) from the Small Main-Belt Asteroid Spectroscopic Survey (SMASS, Xu et al., 1995).

2.3 Photometric correction

In this study, VIR spectra are calibrated to bidirectional reflectance. First, we calculate the reflectance factor (Hapke, 1981), defined as $I/F \times d^2/\pi$, where I is the irradiance from the surface of Ceres that reaches the instrument, F the solar radiant flux, and d is the distance from the Sun to the surface. An accurate estimate of the solar flux at the surface requires measurements of the solar incidence angle at the surface with respect to the topography. Therefore, the conversion from I/F to bidirectional reflectance requires a correction of surface photometric effects, which relies on measurements of the emergence angle with respect to the normal to the surface, and the phase angle. These angles come from evaluation of Ceres' topography, such as the global shape model calculated by Park et al. (2016).

In detail, the correction is performed as follows:

1) In order to calculate geographic coordinates, the incidence, emergence and phase angles, we used the standard Navigation and Ancillary Information Facility (NAIF) SPICE system (Acton, 1996), which contains the attitude and trajectory files of the spacecraft reconstructed a posteriori from telemetry data. For each VIR pixel, we calculated the surface intercept of the line of sight of the IFOV four corners at the beginning and at the end of the data acquisition. The duration of the integration time is important to consider because it accounts for the relative motion of the spacecraft with respect to the surface, and it may eventually represent several times the projected area of the IFOV. More details are provided in Combe et al. (2015).

2) A first correction of photometric effects accounts for the topography at scales larger than the size of a VIR pixel projected at the surface. The Ceres shape model (Park et al., 2016) has higher spatial resolution than VIR, even for LAMO observations. The Akimov disk-function (Akimov, 1975; Shkuratov et al., 1999) is a model that has been proven to be

adequate for the surface of Ceres (Schröder et al., 2016; Li et al., 2016; Longobardo et al., 2016). It is a scalar multiplied by each VIR I/F spectrum.

3) Finally a phase function correction accounts for the physical structure of the surface materials such as surface roughness (performed after correction by the Akimov disk-function). In the case of Ceres, this curve is best fitted by a polynomial function in the logarithmic space. The correction is applied as a vector multiplied to each VIR pixel. We standardize bidirectional reflectances to incidence angles of 0° and emission angles of 30°, which is the common geometry for many laboratory measurements of reflectance spectroscopy (e.g. RELAB, Pieters et al., 1983).

2.4 Search for H_2O-rich materials

Our approach consists of scaling and ratioing VIR spectra. For scaling, we divide each spectrum by its median value in the intervals 1.10-1.40 μm and 1.62-2.40 μm. These ranges avoid instrument artifacts and the effects of thermal emission that occurs at longer wavelengths. Therefore, the median value over this entire range of wavelengths is less sensitive to noise in the data than the value at a given wavelength. This operation minimizes the effects of albedo and possible remaining illumination variations. Because the surface composition of Ceres is very homogenous, with the exception of small, young areas that are spectrally different, it is assumed that, over time, any local component is progressively mixed with remote materials that have an average composition (impact gardening is one process). As a way to minimize the effects of mixture of local components (here, H_2O-rich materials) with the average surface composition, we divide each scaled VIR spectrum by the average scaled spectrum of Ceres (Fig. 1). After this operation, the absorption bands of the local component dominate in the spectra. The division is also an approximation for the effects of intimate mixing that occurs when multiple scattering dominates. This technique is commonly used for the search of absorption bands in spectral analysis of planetary surfaces.

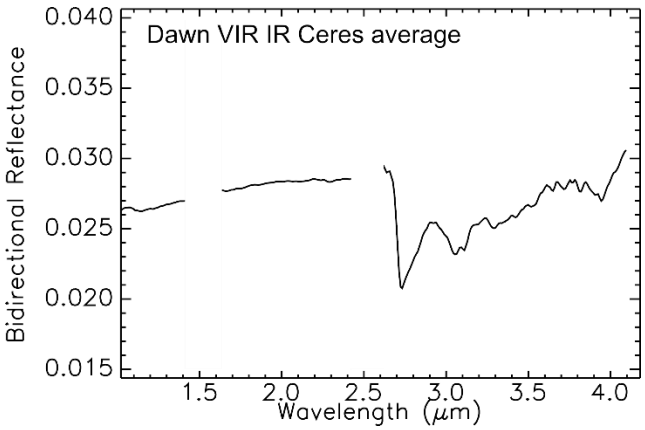

Fig. 1: Ceres average IR spectrum measured by Dawn's VIR IR imaging spectrometer (De Sanctis et al., 2015).

We focused on the search of H_2O ice because this is the only component that has been linked to the identification of H_2O absorption bands in the VIR spectra of Ceres in the Oxo crater (Combe et al., 2016). For an automatic search of H_2O absorption bands, we compared spectra of H_2O-rich materials with ratioed VIR spectra. We used the technique of spectral shape fitting using the Multiple-Endmember Linear Spectral Unmixing Model (MELSUM: Combe et al., 2008). Each VIR spectrum in the ranges 1.1-1.4 μm and 1.6-2.4 μm was modeled by one ratioed VIR spectrum of the Oxo crater's H_2O-rich area used as a spectral endmember, plus a computed straight line (with variable slope and intercept for each pixel) to account for low-albedo, spectrally neutral materials

and possible effects of Ceres' surface photometry that may affect the spectral slope. The analysis of each VIR spectrum is independent. The result is a weighing factor (mixing coefficient) associated to the H_2O-rich spectral endmember, and an estimate of the quality of fit by the Root-Mean Square (RMS). Finally, the H_2O-ice weighing factor divided by the RMS constitutes a very sensitive spectral criterion for the detection of H_2O ice. Above a certain threshold, we noted a sudden increase of the number of VIR spectra selected: this was an indication that the threshold was a limit between two different classes of spectra. As an independent way to assess whether the VIR spectra selected automatically were compatible with H_2O absorption bands or not (false positive), we used visual inspection. We found that the threshold value was an adequate compromise between high sensitivity to the presence of H_2O absorption bands and few occurrences of false positive detections. Finally, the elimination of remaining false positives was done by visual inspection of all VIR spectra above that threshold. In Fig. 6, Fig. 7, Fig. 8 and Fig. 9, the threshold is defined by the value of 1265 in the color ramp.

3. Inventory and surface properties of exposed H_2O-rich areas on Ceres

Nine locations on Ceres were identified as H_2O-rich materials exposed at the surface (Fig. 2). Fig. 3 shows a selection of I/F spectra from single VIR pixels (no averaging) in order to illustrate the amplitude of measurement uncertainties (error bars) compared to the depth of H_2O absorption bands. Error bars are calculated from variations of the dark current, independently for each VIR detector element. For each VIR file, the dark current is measured at least twice: once at the beginning, once at the end, and sometimes in between. Removal of the dark current (*dark* in the equation below) is based on a linear interpolation between the dark current measurements that precede and that follow the acquisition of a targeted signal (a spectrum from the surface in Digital Numbers or *DN*s). For each wavelength, the uncertainty is calculated as follows: $Error = [\max(dark) - \min(dark)] \ / \ [DN - interpolated\ dark]$. This method implies that measured variations of the dark current are representative of the maximum and minimum values of the dark current that actually occurs during the acquisition of a file. It is necessary to make this assumption, because the dark current is not measured before and after each line of a given file. In Fig. 3, each error bar defines the envelope between $(1+Error) \times Spectrum$ and $(1-Error) \times Spectrum$. In the case of multiple observations of the same site, the selection of spectra in Fig. 3 focuses on the earliest detections of H_2O that were acquired during Survey and HAMO, for which the spatial resolution is the lowest and therefore where the H_2O absorption bands are the weakest. In all cases, the absorption band at 2 μm is detected without ambiguity: its amplitude is greater than the measurement uncertainties, and it is visible over a range of wavelengths that corresponds to more than ten wavelength channels.

All H_2O detections are illustrated in Fig. 4 as average bidirectional spectra. Error bars are not shown for clarity. Note that. Table 2 summarizes the characteristics of each site. All areas are located at latitudes above 30°, seven in the northern hemisphere and two in the southern hemisphere. Oxo Crater was the most observed (10 times by VIR) because it was a priority target. Four sites have been observed multiple times by VIR under illumination conditions that were favorable enough to provide spectra with detectable H_2O absorption bands. Fig. 5 shows the same spectra divided by the average spectrum of Ceres and scaled to the average reflectance level between 1.1 and 2.4 μm. All the spectra exhibit absorption bands at 2.0 μm, and most of them also have absorption features at 1.65 and 1.28 μm. The absorption band at 1.28 μm is the weakest of all, and thus it is not always detected when the signal-to-noise ratio is not high enough (Fig. 4 and Fig. 5, for example sites A and H). In five cases, a local maximum is visible at 3.1 μm, which is characteristic of the Fresnel peak of crystalline H_2O ice. Most of the spectra have a negative spectral slope that is also consistent with

H_2O ice as a spectrally dominant component, however this is not systematic because in several cases, the H_2O-rich area is not spatially resolved by VIR, and therefore the areal mixture may not preserve the spectral slope of pure H_2O.

To better describe the surface and identify other possible features potentially related to H_2O, each site was also analyzed using FC clear images. As summarized in Table 2, all of the areas that have H_2O-rich materials exposed at the surface present at least one visible characteristic, such as an albedo higher than the surrounding terrains, a morphology that indicates flow of material, or an adjacent shadow that may be persistent. From these observations, we found that several sites present similar characteristics. A more detailed description of our findings is available in the next four subsections: 3.1) On three occurrences (all in the northern hemisphere, including the Oxo crater), H_2O-rich materials with albedo slightly higher than surrounding terrains are associated with fresh impact craters presenting flow features or persistent shadows. 3.2) The Juling crater is a unique case because the H_2O-rich materials detected by VIR are present on a cliff with a steep pole-facing slope that was not under direct solar illumination at the time of the observations, but was made visible by secondary scattered illumination coming from the opposite crater wall, covered with high-albedo materials. 3.3) Another unique case is a flow feature that is not associated with high albedo materials nor persistent shadows at 61.57°N, 51.82°E. 3.4) Small areas, not spatially resolved by VIR, with high albedo observed by FC, are found in four occurrences, including one in the southern hemisphere (Baltnay Catena).

Fig. 2: Location of exposed H_2O-rich areas on Ceres. The rectangles indicate the boundaries of FC context images displayed in the next figures, and the line style refers to the type of surface feature that is observed. The grey vertical bands and locations marked by an X labeled Region A and Piazzi refer to the two areas identified as possible sources of H_2O vapor outgassing by Küppers et al. (2014). Projection: Simple Cylindrical; central meridian: 0 (adapted from Roatsch et al., 2016).

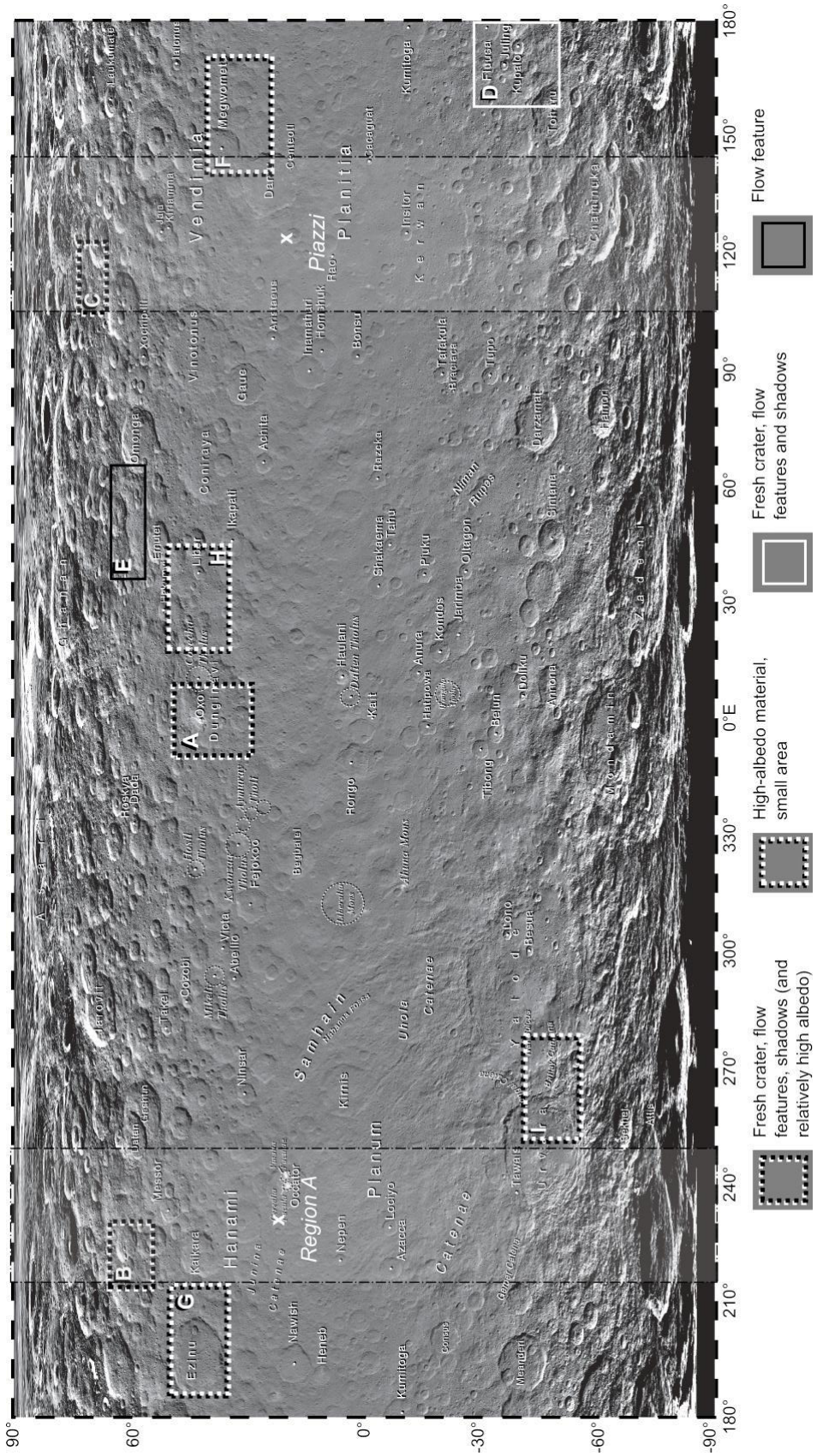
90°
60°
0°
-30°
-60°
-90°
180°
210°
240°
270°
300°
330°
0°E
30°
60°
90°
120°
150°
180°
A
B
C
D
E
F
G
H
I
Region A
Piazzi
Hanami Planum
Vendimia Planitia
Samhain Catenae
Occator
Kerwan
Dantu
Ezinu
Kaikara
Messor
Nepen
Azacca
Lociyo
Kirnis
Ninsar
Takel
Cozobi
Abellio
Vicia
Fejokoo
Begbalel
Rongo
Haulani
Kait
Dada
Oxo
Liber
Ikapati
Conraya
Omonga
Achita
Gaue
Vinotonus
Aristaeus
Inamahari
Bonsu
Xochipilli
Megwomets
Sacaguat
Kumitoga
Insitor
Tupo
Tafakula
Hamori
Darzamat
Sintana
Jarimba
Oltagon
Piuku
Kondos
Anura
Hatipowa
Bejun
Tibong
Dolliku
Annona
Lono
Besua
Tawals
Meanderi
Nawish
Heneb
Urvara
Yalode
Zadeni
Chaminuka
Toharu
Fluusa
Juling
Kupalo
Fresh crater, flow features, shadows (and relatively high albedo)
High-albedo material, small area
Fresh crater, flow features and shadows
Flow feature

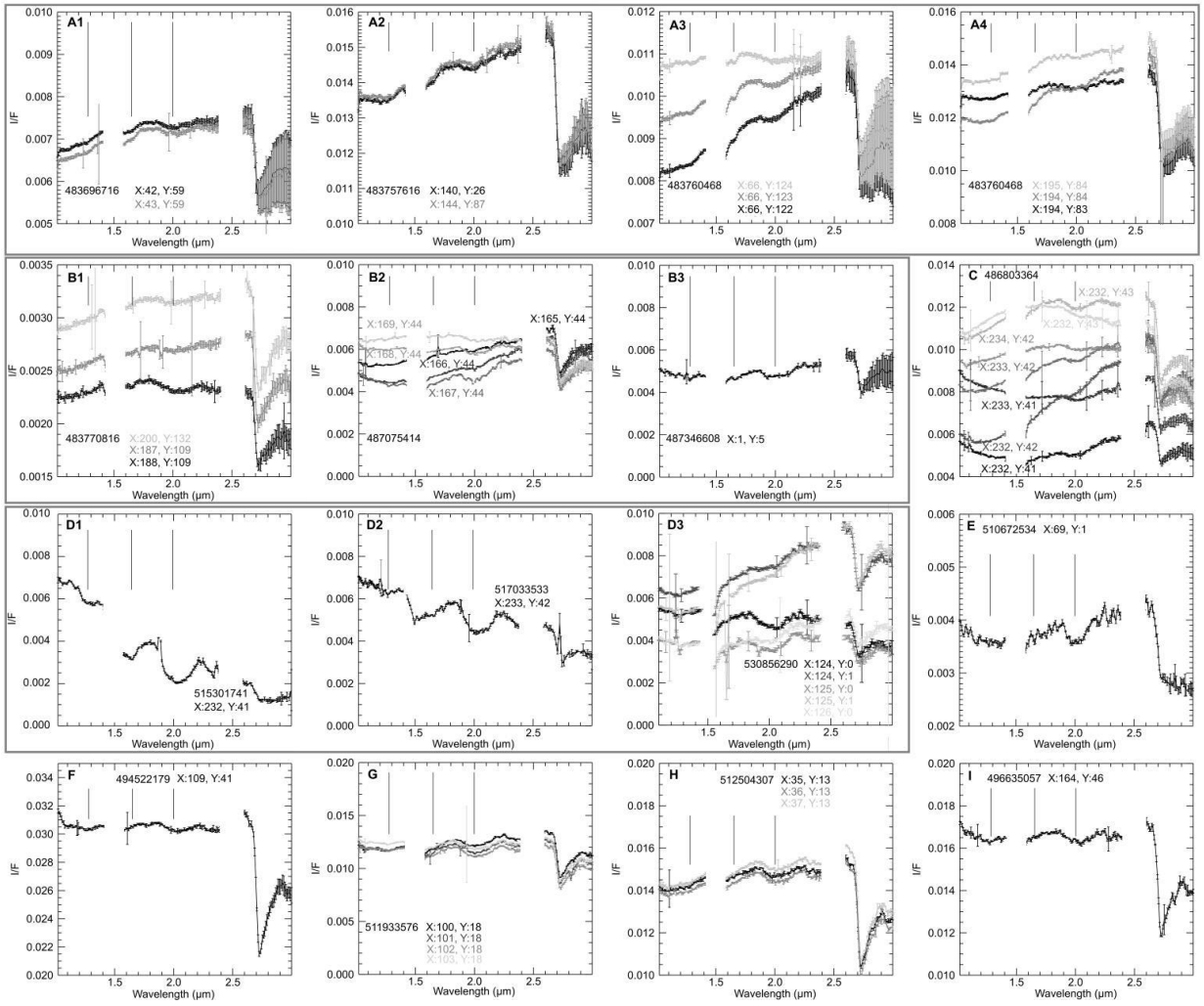

Fig. 3: Selection of VIR IR spectra of all H_2O-rich areas identified on Ceres. Vertical black lines indicate expected locations of H_2O absorption bands at 1.28, 1.65 and 2.0 μm. Each spectrum corresponds to a single VIR pixel. Error bars represent uncertainties related to variations of the dark current for each observation (see text for details). A1-A4 – (41.42°N, 0.76°E) Oxo Crater. B1-B3 – (69.66°N, 114.81°E). C – (61.32°N, 221.06°E). D1-D3 – (-34.83°N, 168.99°E) Juling Crater. E – (61.57°N, 51.82°E) Flow feature (Schmidt et al., 2017). F – (29.60°N, 155.07°E). G – (-47.92°N, 265.46°E) Baltnay Catena. H – (42.20°N, 199.51°E). I – (44.61°N, 32.50°E).

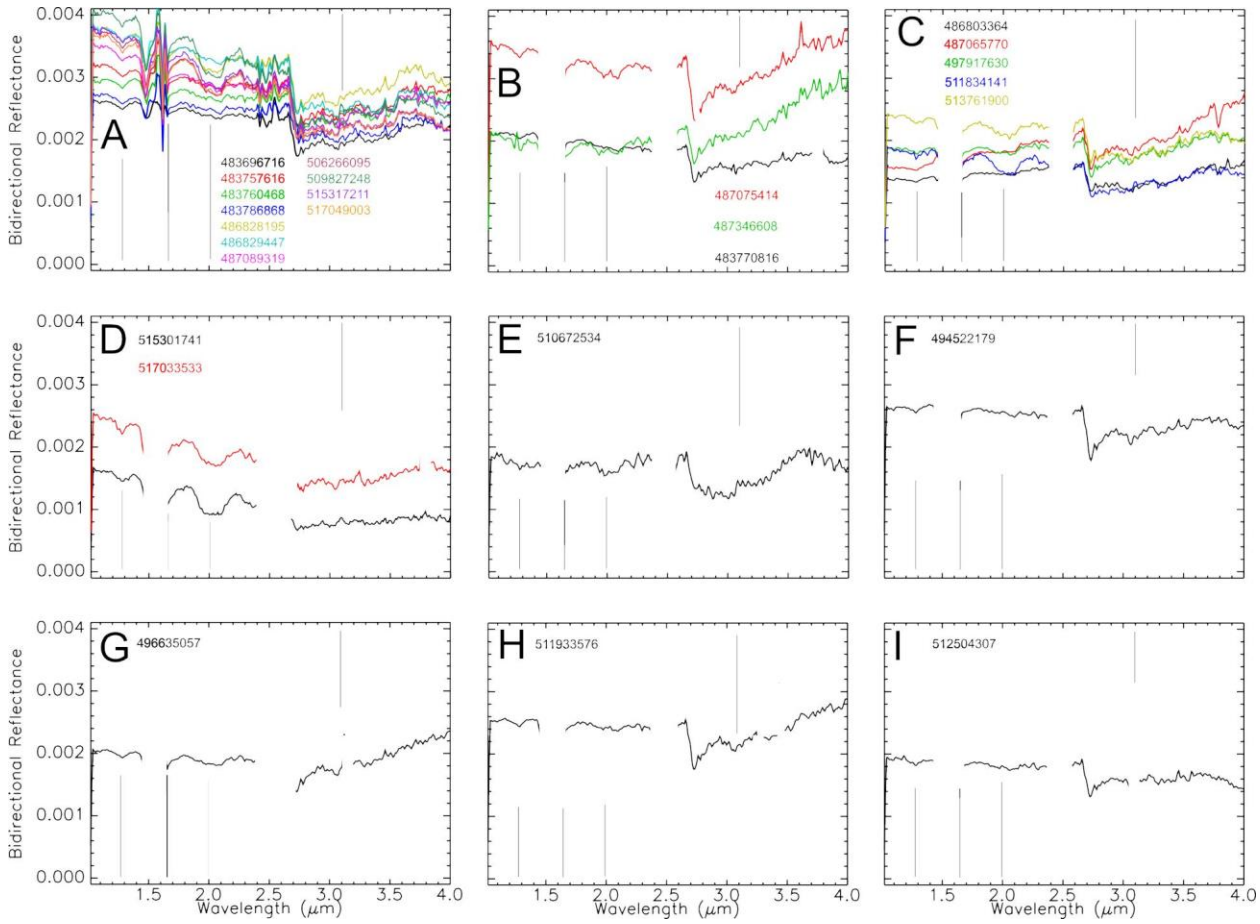

Fig. 4: Average bidirectional reflectance VIR IR spectra of all H_2O-rich areas identified on Ceres. Vertical gray lines indicate expected locations of H_2O absorption bands at 1.28, 1.65 and 2.0 μm, as well as the position of the Fresnel peak of crystalline H_2O ice 3.1 μm. The number of pixels per average spectrum is documented in Table 2. A – (41.42°N, 0.76°E) Oxo Crater. B – (69.66°N, 114.81°E). C – (61.32°N, 221.06°E). D – (-34.83°N, 168.99°E) Juling Crater. E – (61.57°N, 51.82°E) Flow feature (Schmidt et al., 2017). F – (29.60°N, 155.07°E). G – (-47.92°N, 265.46°E) Baltnay Catena. H – (42.20°N, 199.51°E). I – (44.61°N, 32.50°E).

313 **Table 2: Summary of all detections of exposed H_2O at the surface of Ceres by VIR.**

Label in Fig. 4 and Fig. 5	Latitude °N	Longitude °E	Feature name	High albedo under sunlight	Morphological flow feature	Adjacent to shadowed, high-albedo areas	Spatially resolved with VIR	Area estimate from FC (m^2)	Area estimate from VIR (m^2)	Number of H_2O detections by VIR	VIR file names of H_2O detections
A	41.42	0.76	Oxo Crater	Yes	Yes	Yes	Yes		6.8×10^6	9	483757616 483760468 483786868 486828195 486829447 487089319 506266095 509827248 515317211 517049003
B	69.66	114.81		Yes	Yes	Yes	Yes		$< 3.3 \times 10^6$ (1 Survey pixel)	3	483770816 487075414 487346608
C	61.32	221.06	Messor Crater	Yes	Yes	Yes	Yes		1.4×10^6	5	486803364 487065770 497917630 511834141 513761900
D	-34.83	168.99	Juling Crater		Yes	Yes	Yes		Measured: 3.2×10^6 Extrapolated: 6×10^6	6	515301741 517033533 529971002 530038462 530855493 530856290
E	61.57	51.82			Yes		Yes (flow)		$< 1.0 \times 10^4$ (1 LAMO pixel)	1	510672534
F	29.60	155.07		Yes				$1.0 \times 10^4 \pm 6 \times 10^3$	$< 1.2 \times 10^6$ (1 HAMO pixel)	1	494522179
G	42.20	199.51	Ezinu Crater	Yes				$1.5 \times 10^4 \pm 3 \times 10^3$	$< 1.0 \times 10^4$ (1 LAMO pixel)	1	511933576
H	44.61	32.50		Yes				$5 \times 10^3 \pm 2 \times 10^2$	$< 1.0 \times 10^4$ (1 LAMO pixel)	1	512504307
I	-47.92	265.46	Baltay Catena	Yes				$2.8 \times 10^4 \pm 6 \times 10^3$	$< 1.2 \times 10^6$ (1 HAMO pixel)	1	496635057

314 **Table 2 (continued)**

VIR file name	Number of VIR spectra showing H_2O absorptions	Start Time	Dawn at Ceres mission phase	Target Center Distance (km)	Sub-solar latitude (°)	Incidence Angle (°)	Emergence Angle (°)	Pixel Scale (m)	Label in Fig. 4 and Fig. 5
483757616	2	2015-05-01T13:05:50	RC3'	14067.0	3.871	61	46	3462	A
483760468	8	2015-05-01T13:53:22	"	14067.8	3.872	54	44	3456	
483786868	3	2015-05-01T21:13:22	"	14075.2	3.873	43	19	1100	
486828195	11	2015-06-06T02:02:09	Survey	4859.7	3.976	37	10	1099	
486829447	26	2015-06-06T02:23:01	"	4859.8	3.976	53	1	1101	
487089319	24	2015-06-09T02:34:13	"	4858.2	3.983	57	3	94	
506266095	101	2016-01-17T01:27:06	LAMO	840.4	3.383	44	14	96	
509827248	236	2016-02-27T06:39:39	"	841.9	3.064	62	32	99	
515317211	107	2016-04-30T19:39:02	"	844.1	2.464	53	22	102	
517049003	128	2016-05-20T20:42:14	"	854.6	2.251	69	16	1103	
483770816	3	2015-05-01T16:45:50	RC3	14070.8	3.872	31	69	3463	B
487075414	2	2015-06-08T22:42:28	Survey	4856.5	3.982	69	4	1102	
487346608	1	2015-06-12T02:02:22	"	4856.6	3.988	55	16	95	
486803364	1	2015-06-05T19:08:18	Survey	4856.7	3.976	65	18	1107	C
487065770	2	2015-06-08T20:01:44	"	4855.7	3.982	60	49	388	
497917630	2	2015-10-12T10:26:02	HAMO	1936.9	3.89	70	12	100	
511834141	43	2016-03-21T12:07:52	LAMO	850	2.859	69	17	101	
513761900	17	2016-04-12T19:37:11	"	849.8	2.646	31	69	3463	
515301741	76	2016-04-30T15:21:12	LAMO	838.6	2.466	52	17	100	D
517033533	5	2016-05-20T16:24:24	"	859.8	2.253	68	3	99	
529971002	18	2016-10-17T10:08:53	CXJ	1963.5	0.375	54	15	377	
530038462	34	2016-10-18T04:53:13	"	1963.8	0.364	44	30	390	
530855493	46	2016-10-27T15:50:23	"	1963.6	0.233	43	34	390	
530856290	5	2016-10-27T16:03:40	"	1962.8	0.233	41	38	392	

510672534	1	2016-03-08T01:27:45	LAMO	851.3	2.979	43	21	376	E
494522179	1	2015-09-03T03:15:11	HAMO	1940.4	3.992	55	8	97	F
511933576	5	2016-03-22T15:45:07	LAMO	846.9	2.848	54	10	94	G
512504307	3	2016-03-29T06:17:18	LAMO	840.1	2.787	75	49	389	H
496635057	1	2015-09-27T14:09:49	HAMO	1936.9	3.936	80	39	3427	I

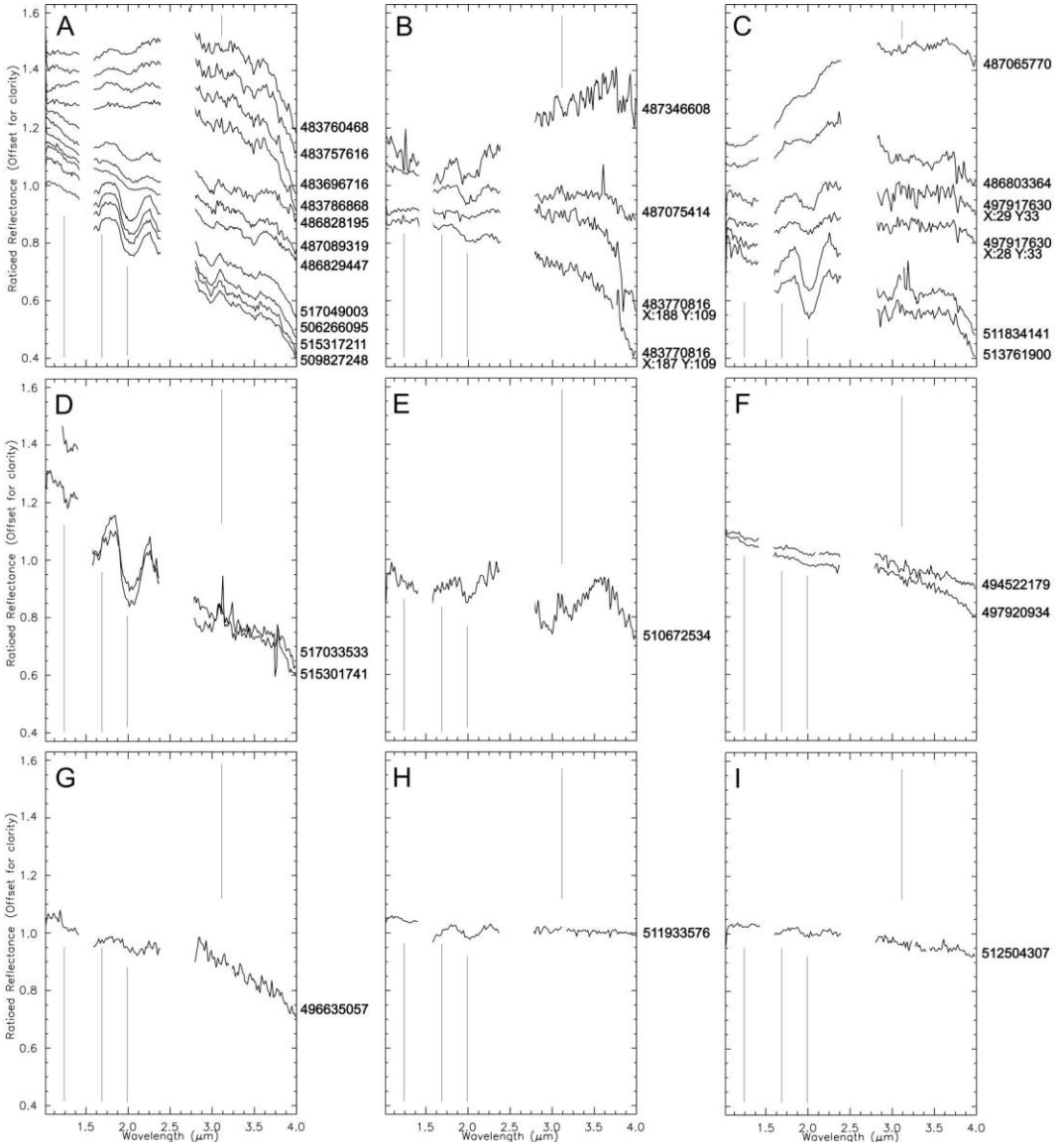

Fig. 5: Average ratioed and scaled reflectance VIR IR spectra of all H_2O-rich areas identified on Ceres. Vertical gray lines indicate expected locations of H_2O absorption bands at 1.28, 1.65 and 2.0 μm, as well as the position of the Fresnel peak of crystalline H_2O ice 3.1 μm. A – (41.42°N, 0.76°E) Oxo Crater. B – (69.66°N, 114.81°E). C – (61.32°N, 221.06°E). D – (-34.83°N, 168.99°E) Juling Crater. E – (61.57°N, 51.82°E) Flow feature (Schmidt et al., 2017). F – (29.60°N, 155.07°E). G – (-47.92°N, 265.46°E) Baltnay Catena. H – (42.20°N, 199.51°E). I – (44.61°N, 32.50°E).

3.1 Fresh crater, flow features, shadows and relatively high-albedo

Fig. 6, Fig. 7 and Fig. 8 illustrate three H_2O-rich locations detected by VIR that have similar characteristics. These sites are located at latitudes higher than 42°, all in the northern hemisphere. They are all associated with fresh impact craters, as shown by the sharp rim crests and the boulders just outside the rim. They all contain material with higher albedo than the surrounding terrain whose

location corresponds to the detection of H_2O absorption bands by VIR. In addition, these high-albedo surfaces correspond to crater wall material, near lobate flows, suggesting that they are affected by mass wasting or slope movements. In all three cases, the illuminated, H_2O-rich and high-albedo surface is on a pole-facing slope and adjacent to shadowed high-albedo areas, as revealed by FC images displayed in logarithmic scale. The upper parts of the wall, which have also high albedo, do not contain measurable H_2O absorption bands.

H_2O was previously detected in the 9.2-km diameter Oxo Crater (Combe et al., 2016). Since the first detection of H_2O in Oxo Crater made with Survey data, VIR made several subsequent targeted observations from LAMO, which are illustrated in color in Fig. 6. The improvement in spatial resolution (~ 100 m/pixel, which is about 10 times higher than images acquired in Survey) allows several, isolated H_2O-rich zones to be detected, and the total area of the H_2O-rich materials (6.8 x 10^6 m^2) to be evaluated more accurately. In this data, H_2O is now clearly associated with surface materials with slightly higher albedo than adjacent terrains.

The second location is a 5.5-km diameter crater at 69.66°N, 114.81°E, where persistent shadows are combined with high-albedo materials (Platz et al., 2016; Ermakov et al., 2017) (Fig. 7). This crater was observed by VIR three times, exclusively from Survey orbit, and the H_2O absorption bands are present in only one or two VIR pixels each time. Each of these few VIR pixels cover most of the crater, as well as surrounding areas. Because of the similarity with the other two craters, we make the hypothesis that H_2O-rich materials have often relatively higher albedo than its surrounding terrains, and are adjacent to shadowed areas in the crater floor.

In this study, we identified a third crater (Fig. 8) at 61.32°N, 221.06°E that is 6.1 km in diameter, where H_2O has been detected by VIR from Survey, HAMO and LAMO orbits. Only VIR LAMO pixels are illustrated in color in Fig. 8.

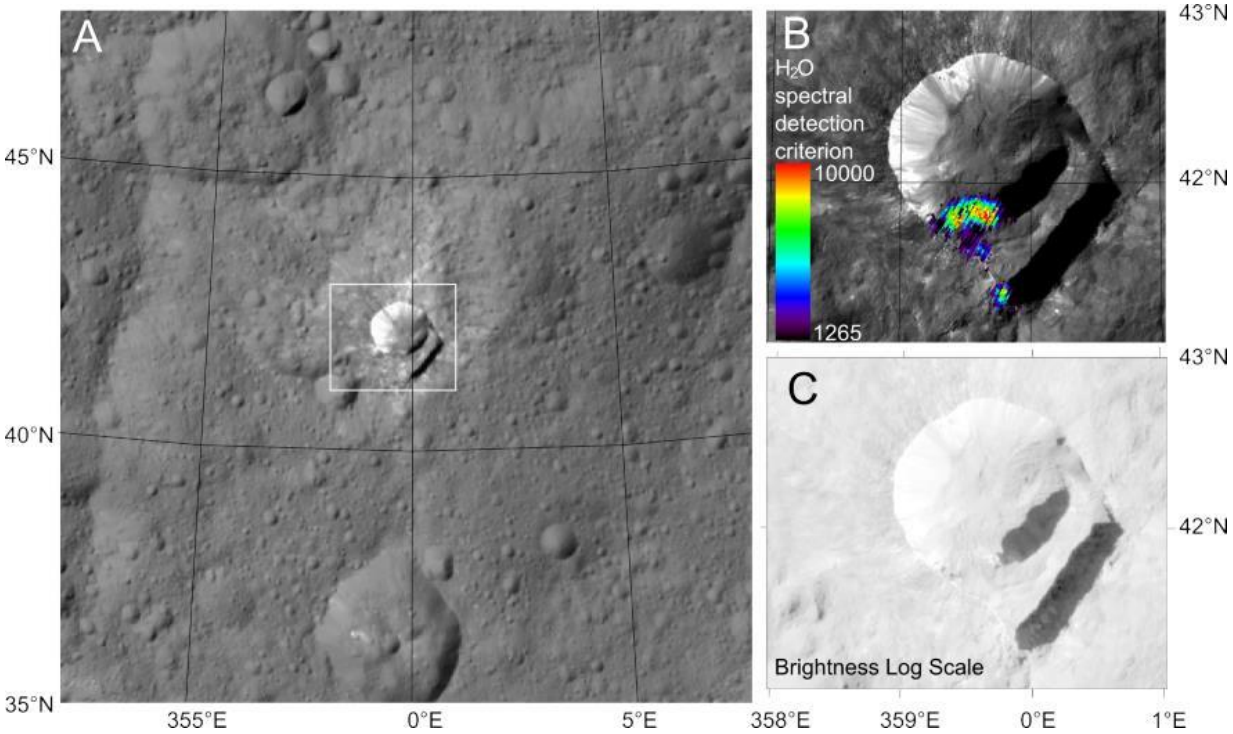

Fig. 6: FC imagery context of the H_2O-rich material area at 41.42°N, 0.76°E associated to Oxo Crater and southeastern scarp. A – Mosaic from HAMO observations displayed in Lambert conformal conic projection. The white rectangle delimits the close-up view on the right. B – Close-up view of Oxo crater from image FC21A0052044_16017012741F1F acquired from LAMO. Colored pixels represent VIR H_2O detections of H_2O

from LAMO. Values are mixing coefficients divided by the RMS (i.e., the quantity that was used to identify H_2O from VIR spectra). C – Same FC image as B, with brightness display stretched in logarithmic scale in order to visualize both illuminated and shadowed areas.

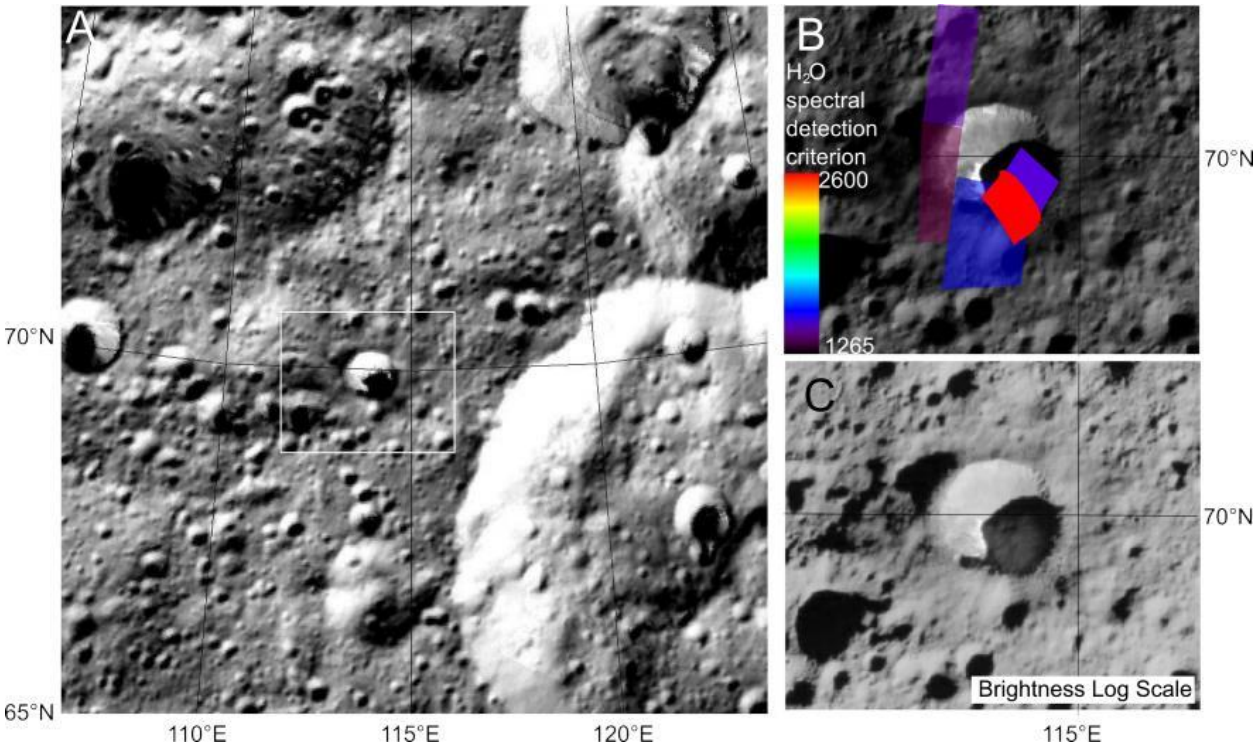

Fig. 7: FC imagery context of the H_2O-rich material area at 69.66°N, 114.81°E inside a fresh impact crater (Platz et al., 2016). A – Mosaic from HAMO observations displayed in Lambert conformal conic projection. The white rectangle delimits the close-up view on the right. B – Close-up view of the fresh crater from image FC21A0046607_15351072425F1D acquired from LAMO. Colored pixels represent VIR H_2O detections of H_2O from LAMO. Values are mixing coefficients divided by the RMS (i.e., the quantity that was used to identify H_2O from VIR spectra). C – Same FC image as B, with brightness display stretched in logarithmic scale in order to visualize both illuminated and shadowed areas.

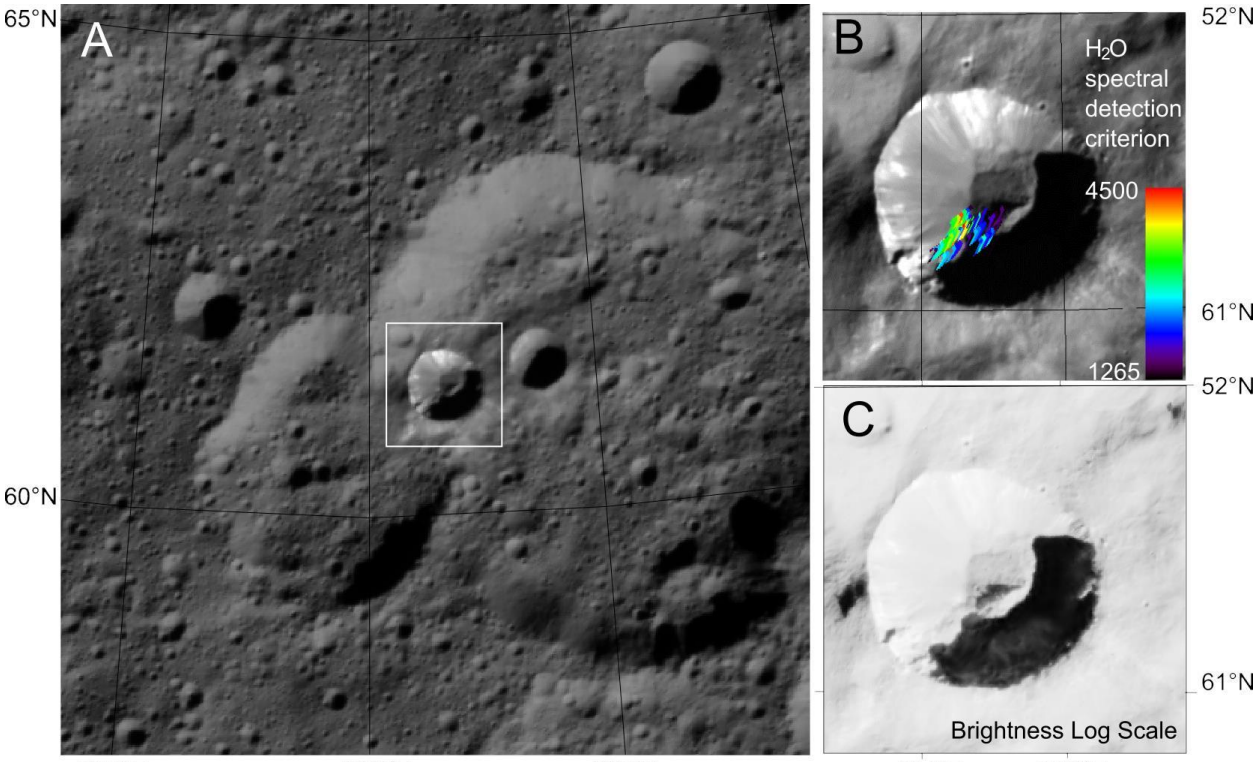

Fig. 8: FC imagery context of the H_2O-rich material area at 61.32°N, 221.06°E inside a fresh impact crater included in Messor Crater (Combe et al., 2017). A – Mosaic from HAMO observations displayed in Lambert conformal conic projection. The white rectangle delimits the close-up view on the right. B – Close-up view of the fresh crater from image FC21A0047863_15358091114F1G acquired from LAMO. Colored pixels represent VIR H_2O detections of H_2O from LAMO. Values are mixing coefficient divided by the RMS (i.e., the quantity that was used to identify H_2O from VIR spectra). C – Same FC image as B, with brightness display stretched in logarithmic scale in order to visualize both illuminated and shadowed areas.

3.2 Fresh crater, flow features and shadows

Juling Crater (Fig. 9) is only one of the two sites in the southern hemisphere where exposed H_2O-rich materials were found (De Sanctis et al., 2016). The H_2O-rich materials are found in two VIR LAMO observations, and are all located near the top of northern wall. This is the place with the second most intense H_2O absorption bands on Ceres after LAMO observations of Oxo. In the FC image, most of the crater wall's surface is in the shadow, and it is only visible because of scattered light from adjacent terrains and the opposite wall, which is covered by high-albedo materials.

According to FC observations, the northern, pole-facing wall has steep slopes and a sharp scarp. At the base of the wall, a smooth material with steep margins, longitudinal grooves and lobate in planar view extends toward the crater center, which is consistent with some sort of material flow. H_2O-rich materials correspond to the sharp scarp and therefore may have their source directly on the wall, where mass wasting exposes fresh material. This suggests that H_2O is present in the subsurface in the immediate vicinity of the crater, at least on the northern side. Alternatively, the H_2O-rich area has topography that looks like it would shadow the pole-facing wall regardless of the time of day; therefore, if it is shadowed a large fraction of the time, it might be a potential site for cold trapping of water molecules.

The upper part of the illuminated opposite wall and rim have high albedo but they do not contain H_2O, according to VIR spectra.

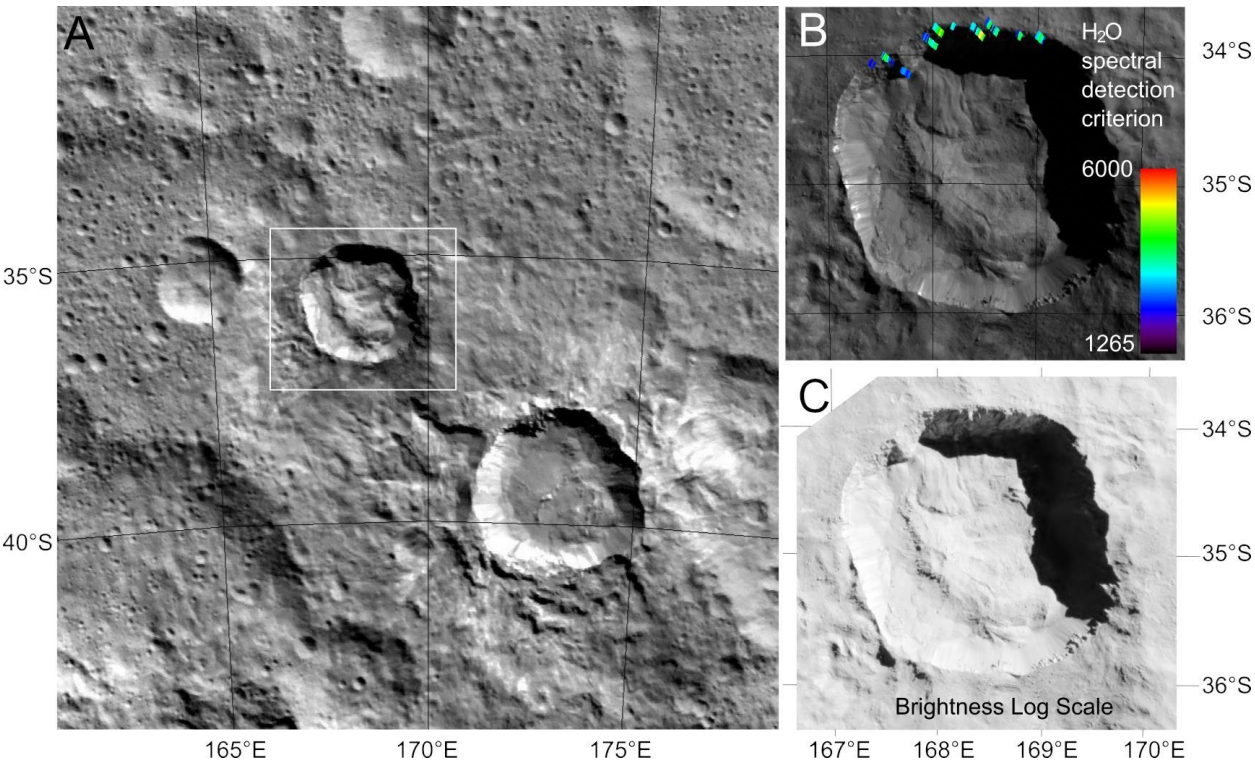

Fig. 9: FC imagery context of the H_2O-rich material area at 34.83°S, 168.99°E on the northern cliff of the Juling crater. A – Mosaic from HAMO observations displayed in Lambert conformal conic projection. The white rectangle delimits the close-up view on the right. B – Close-up view of the Oxo crater from image FC21A0052009 acquired from LAMO. Colored pixels represent VIR H_2O detections of H_2O from LAMO. Values are mixing coefficients divided by the RMS (i.e., the quantity that was used to identify H_2O from VIR spectra). C – Same FC image as B, with color display stretched in order to enhance the contrast within the shadowed area.

3.3 Flow feature with moderate albedo

Fig. 10 shows an 8-km long flow feature, identified among other ones by Schmidt et al. (2017), which is not associated with a fresh impact crater and does not present high-albedo materials. H_2O is detected on a small area (a single VIR pixel from LAMO) in the middle of this flow feature, adjacent to a shadowed area. The spectrum (Fig. 4E and Fig. 5E) exhibits an absorption band at 2.0 μm and a peak at 3.1 μm, which is consistent with the Fresnel peak in crystalline H_2O ice. Analysis of brightness variations within the shadowed areas does not indicate the presence of high-albedo materials. This flow feature is one case among others that initiates from an old and degraded crater rim and progresses downward towards the floor. Both the front and side boundaries of the flow are steep; a longitudinal ridge delimits the sides. According to Schmidt et al. (2017), these types of features occur at high latitudes (predominantly above 50°) and are characteristic of ice-cemented materials. Several impact craters are present on the flow itself, which suggest a flow feature that is old compared to the ones described in sections 3.1 and 3.2. Since H_2O is detected only on a small area of the flow, this suggests that H_2O is present in the bulk of the flow, but is not generally exposed. This observation may imply that H_2O was probably at the surface during the evolution of Ceres, then sublimation obliterated all of it, making it spectrally undetectable. At present, the flow may be covered by a lag deposit that masks most of the ice, assuming the composition is a mixture of H_2O ice and mineral particles. This interpretation is supported by the fact that the surface of the large flow is cratered, except the small area where the detection occurs (upslope on the crater wall,

where the surface is smooth and fresher). The local detection of H_2O by VIR may reveal an episodic exposure of H_2O ice, either from an impact (although no evidence is visible), or from mechanical disturbance of the surface due to movement of the flow, or from ice sublimation.

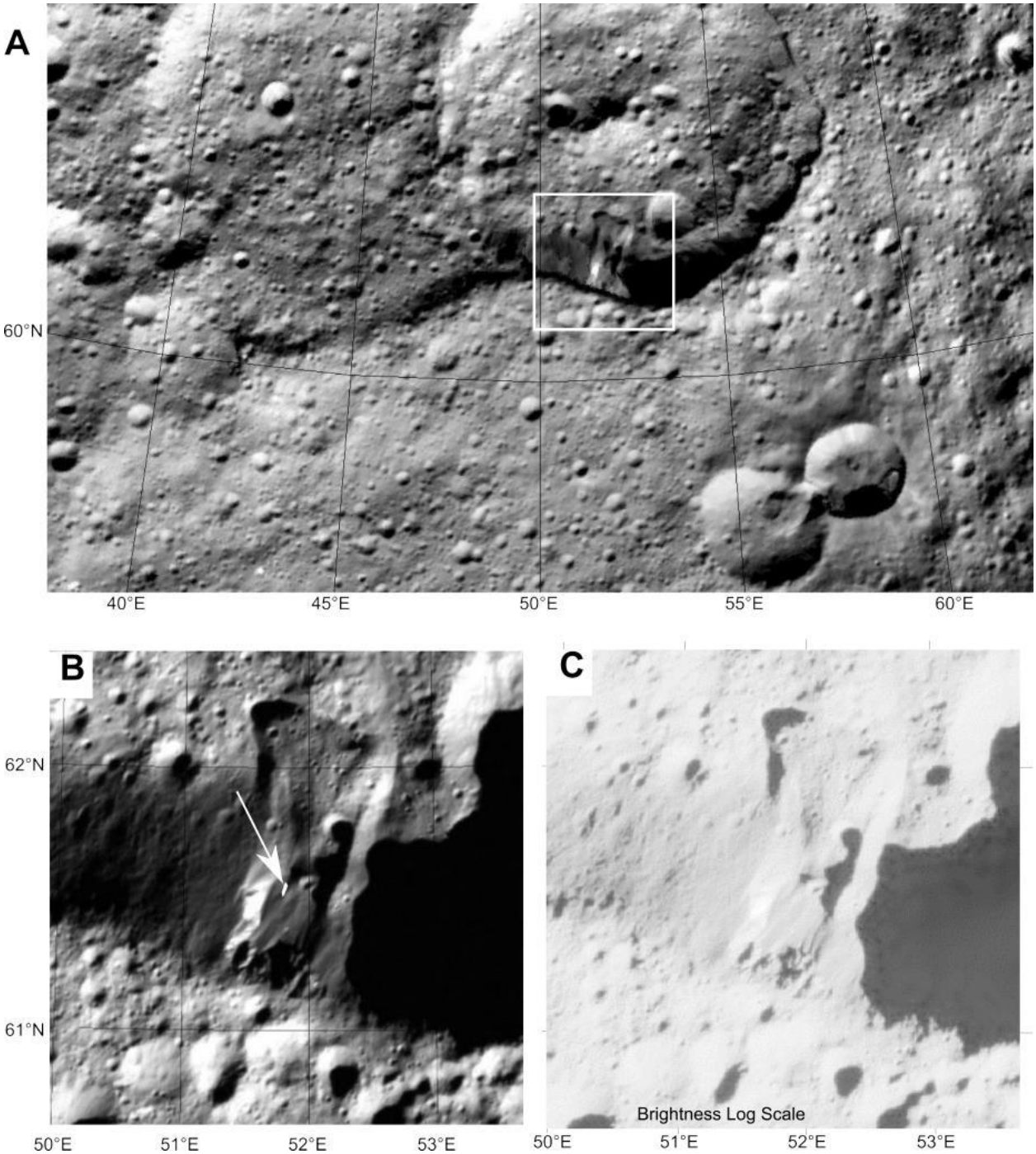

Fig. 10: FC imagery of the H_2O-rich material area at 61.31°N, 51.82°E displayed in Lambert conformal conic projection (Schmidt et al., 2017). A – Mosaic from HAMO observations. The white rectangle delimits the close-up view on the right. B – Close-up view of the flow-like feature that exhibits H_2O absorption bands in one VIR spectrum (in white, at the tip of the arrow) from observation 510672534, displayed in white, superimposed on a projected FC image (FC21A0048919_15363202934F1G). C – Same FC image as B, with color display stretched in order to enhance the contrast within the shadowed area.

3.4 Small, high-albedo areas under direct sunlight

The last type of H_2O-rich areas that we identified is small (<0.1 km^2) and of high-albedo area, whereas the morphology does not indicate a nearby flow feature, and the illumination conditions do not indicate persistent shadows. Four sites present similar traits, although only three of them seem to be associated with the pole-facing slope of a small impact crater. Although VIR does not spatially resolve any of these areas, the detection of H_2O is systematically associated with small high-albedo areas that can be observed with the FC images. All these sites were identified in FC images acquired in HAMO, although none of them were spatially resolved. However, multiple LAMO FC images are available for all of them, where the albedo feature is always spatially resolved and is covered by several pixels. Fig. 11A presents the context FC imagery of the site at 42.20°N, 199.51°E within the Ezinu crater, Fig. 11B illustrates the first FC HAMO observation where the albedo feature is visible, and Fig. 11C shows the first LAMO image. Table 3 lists all images displayed in Fig. 11. A similar case was found at 29.60°N, 155.08°E, where FC images are shown in Fig. 12, and Table 4 provides image information. A third site at 47.92°S, 265.46°E near Baltnay Catena (Fig. 13) resembles the two aforementioned sites, except that it comprises three distinct spatially-resolved areas of high albedo, and possibly four secondary high-albedo areas that are not spatially resolved in FC images. Table 5 provides information for the FC images. The fourth site at 44.61°N, 32.50°E has also a small area of higher albedo (Fig. 14), however, unlike the previous three, it is difficult to identify an impact crater in the FC LAMO images (Table 6).

In all four cases, the high-albedo material was observed consecutively for about one terrestrial year ($1/5^{th}$ of one Ceres year). HAMO observations began for solar longitudes ~95°, shortly after summer solstice (where solar longitude Ls = 90°), and the last LAMO observations were acquired at Ls~160°, which is before the autumn equinox.

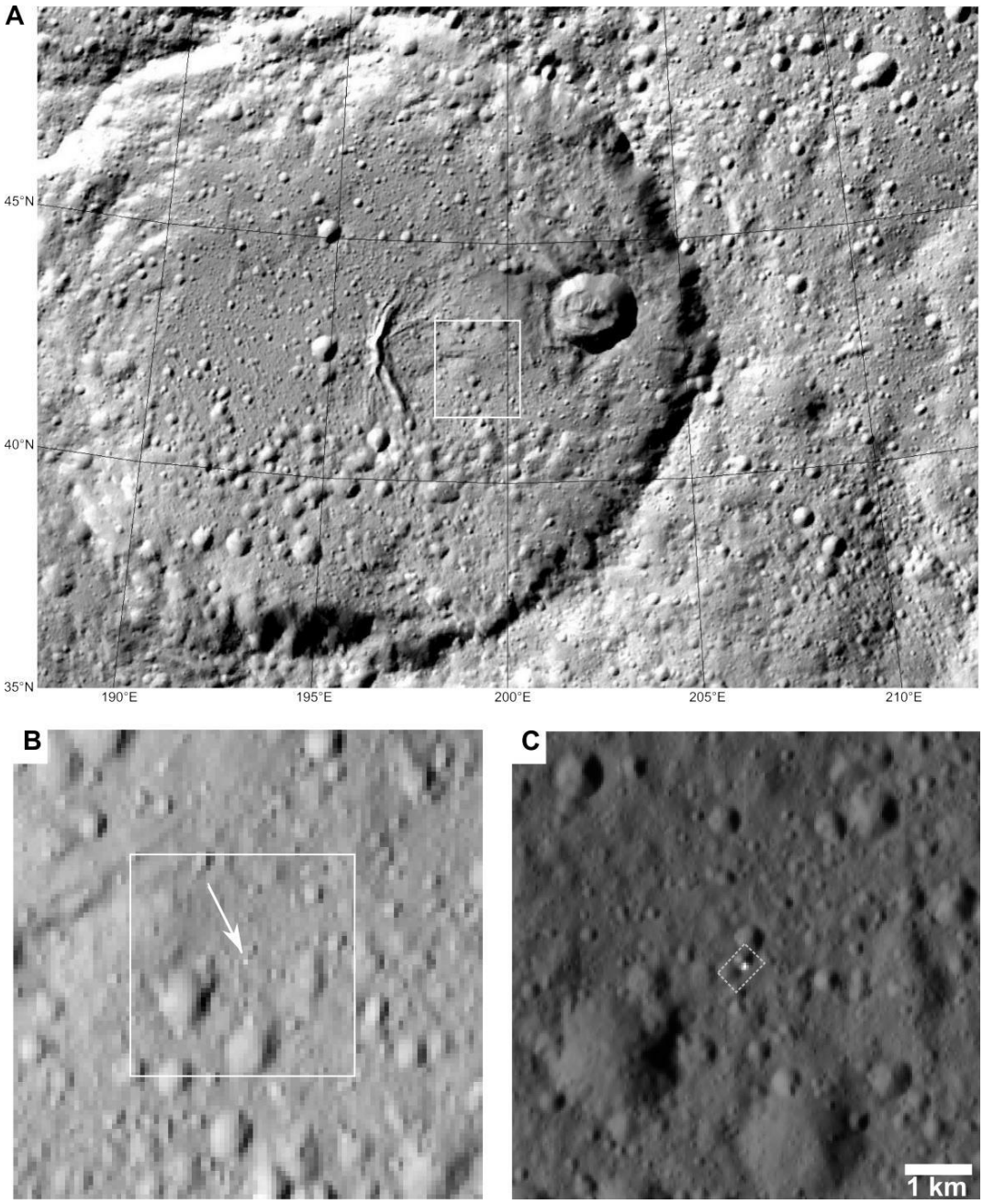

Fig. 11: FC imagery context of the H_2O-rich material area at 42.20°N, 199.51°E within the Ezinu crater (Combe et al., 2017). A – Mosaic displayed in Lambert conformal conic projection. The white rectangle delimits the close-up view on the right. B – Close-up view from the earliest observation of the high-albedo area (white arrow) with FC from HAMO: unprojected portion of FC21B0042226_15245075026F1E. C – Framing Camera LAMO unprojected portion of FC21B0052773_16021091525F1E of the H_2O-rich material area at 42.20°N, 199.51°E. The polygon indicates the footprint of the VIR pixels. Data information and scale are provided in Table 3.

Table 3: Description of the Framing Camera HAMO and LAMO observations of the H_2O-rich material area at 42.20°N, 199.51°E.

Figure Number	Framing Camera file name	Time	Pixel Scale (m)	Solar Longitude (°)
Fig. 11B	FC21B0042226_15245075026F1E	2015-09-02T07:50:26	142	97.47
Fig. 11C	FC21B0052773_16021091525F1E	2016-01-21T09:15:25	34.86	123.59

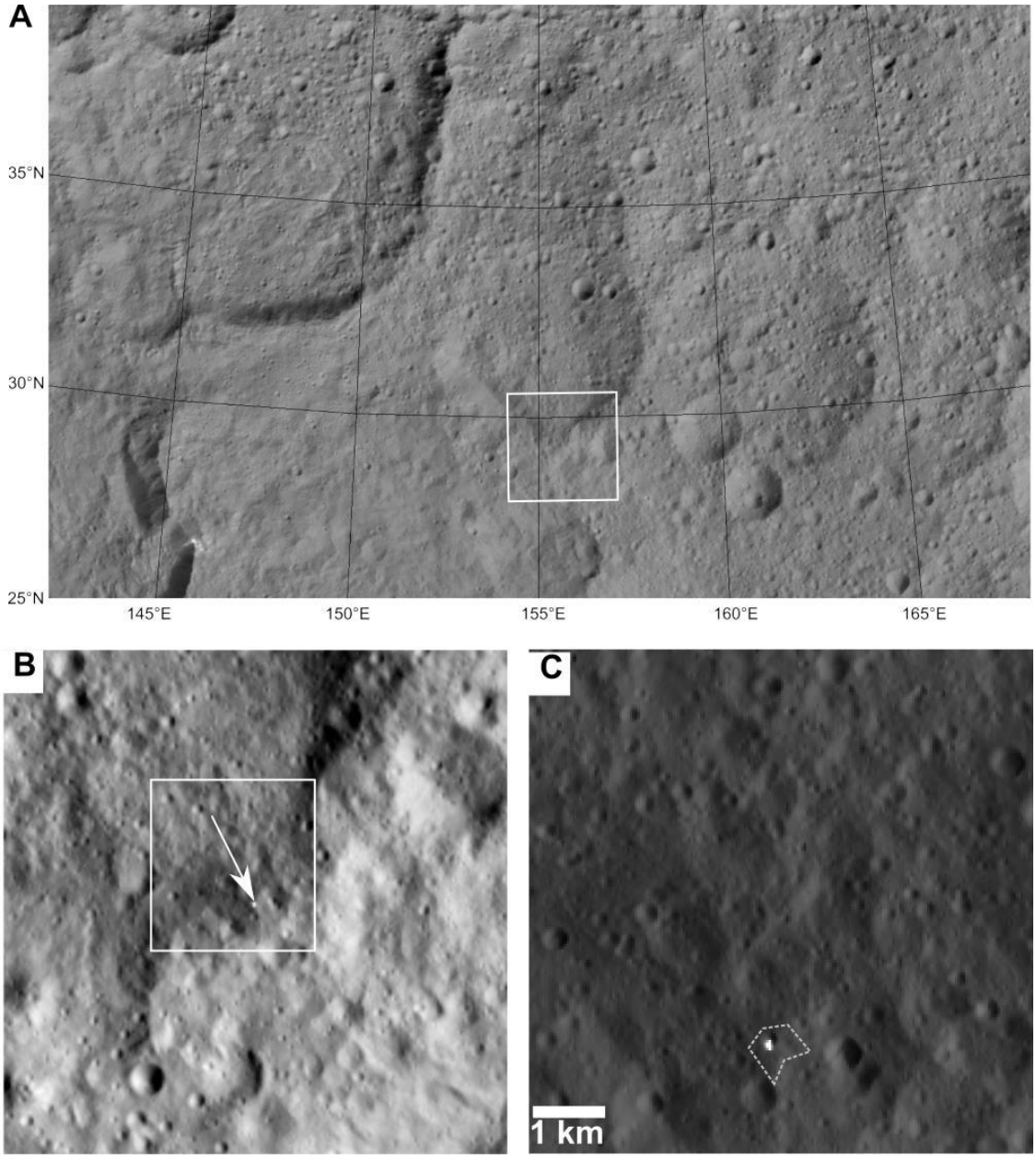

Fig. 12: FC imagery context of the H_2O-rich material area at 29.60°N, 155.08°E. A – Mosaic displayed in Lambert conformal conic projection. The white rectangle delimits the close-up view on the right. B – Close-up view from the earliest observation of the high-albedo area (white arrow) with FC from HAMO: unprojected portion of FC21B0041475_15237105237F1G. C – Framing Camera LAMO unprojected portion of FC21A0046904_15353034740F1G of the H_2O-rich material area at 29.60°N, 155.08°E. The polygon indicates the footprint of the VIR pixel. Data information and scale is provided in Table 4.

Table 4: Description of the Framing Camera LAMO observations of the H_2O-rich material area at 29.60°N, 155.08°E.

Figure Number	Framing Camera file name	Time	Pixel Scale (m)	Solar Longitude (°)
Fig. 12B	FC21B0041475_15237105237F1G	2015-08-25T10:52:37	137	95.99
Fig. 12C	FC21A0046904_15353034740F1G	2015-12-19T03:47:40	36.16	117.46

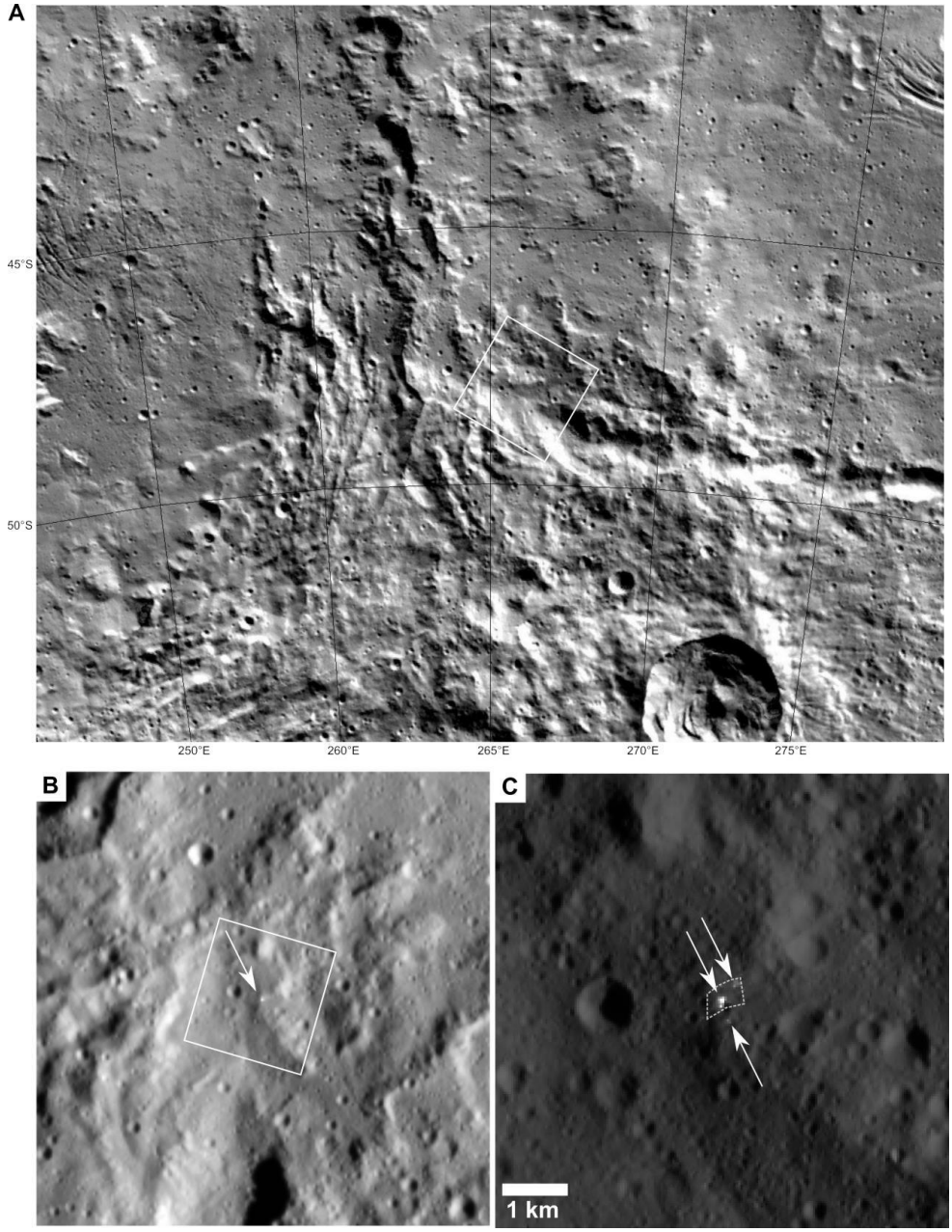

Fig. 13: FC imagery context of the H_2O-rich material area at 47.92°S, 265.46°E. A – Mosaic displayed in Lambert conformal conic projection. The white rectangle delimits the close-up view on the right. B – Close-up view from the earliest observation of the high-albedo area (white arrow) with FC from HAMO: unprojected portion of FC21B0039530_15230123844F1G. C – Framing Camera LAMO unprojected portion of FC21B0049218_16001154324F1D of the H_2O-rich material area at 47.92°S, 265.46°E, near Baltnay Catena. The polygon indicates the footprint of the VIR pixel, and the arrows points at three distinct small, high-albedo features. Data information and scale is provided in Fig. 13.

Table 5: Description of the Framing Camera LAMO observations of the H_2O-rich material area at 47.92°S, 265.46°E, near Baltnay Catena.

Figure Number	Framing Camera file name	Time	Pixel Scale (m)	Solar Longitude (°)
Fig. 13B	FC21B0039530_15230123844F1G	2015-08-18T12:38:44	138	94.69
Fig. 13C	FC21B0049218_16001154324F1D	2016-01-01T15:43:24	34.32	119.95

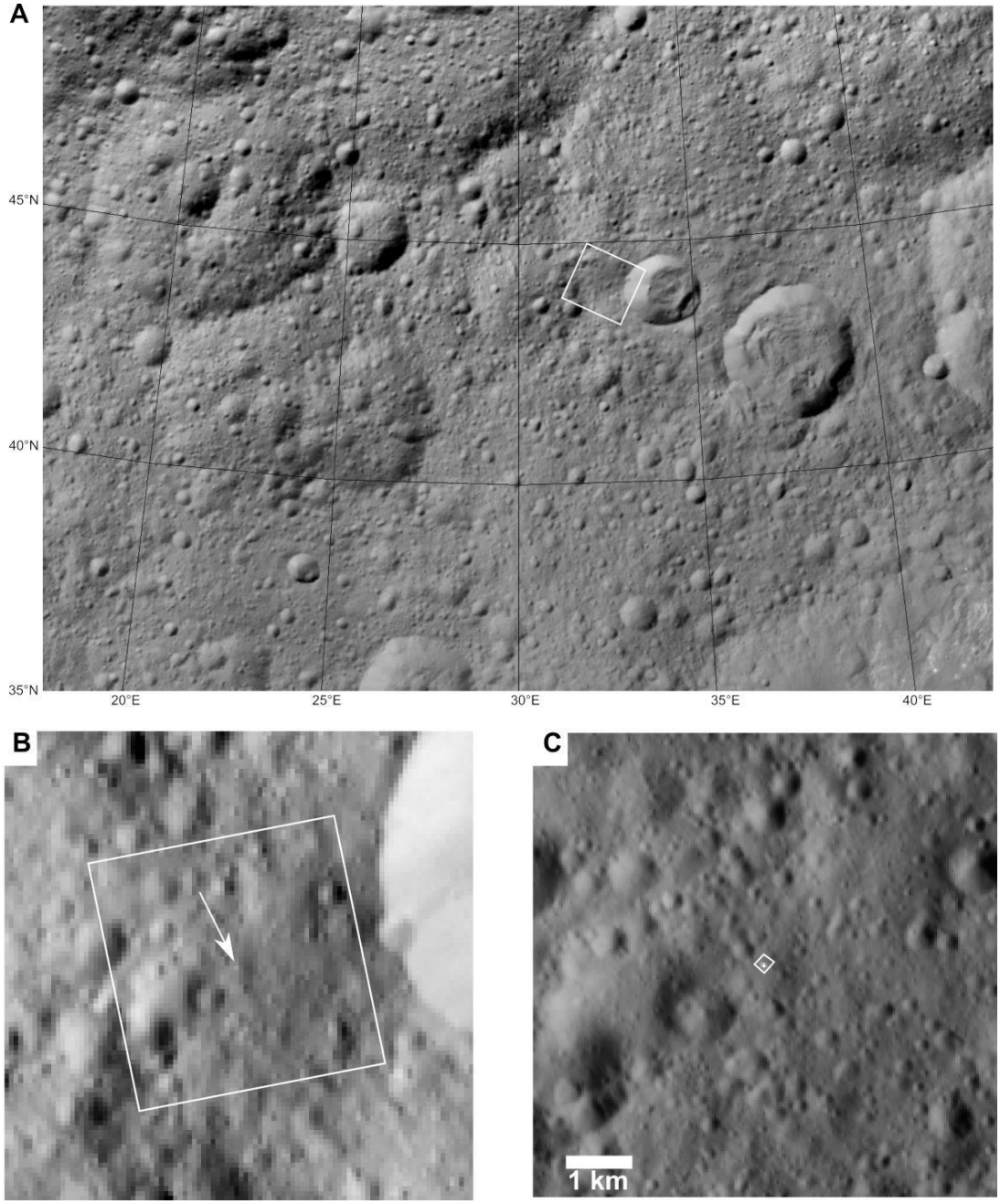

Fig. 14: FC imagery context of the H_2O-rich material area at 44.61°N, 32.50°E. A – Mosaic displayed in Lambert conformal conic projection. The white rectangle delimits the close-up view on the right. B – Close-up view from the earliest observation of the high-albedo area (white arrow) with FC from HAMO: unprojected portion of FC21B0039801_15231214233F1G. C – Framing Camera LAMO unprojected portion of FC21B0046455_15350152140F1A of the H_2O-rich material area at 44.61°N, 32.50°E. The polygon indicates the footprint of the VIR pixel. Data information and scale is provided in Table 6.

Table 6: Description of the Framing Camera LAMO observations of the H_2O-rich material area at 44.61°N, 32.50°E.

Figure Number	Framing Camera file name	Time	Pixel Scale (m)	Solar Longitude (°)
Fig. 14B	FC21B0039801_15231214233F1G	2015-08-19T21:42:33	138	94.95
Fig. 14C	FC21B0046455_15350152140F1A	2015-12-16T15:21:40	36.77	117.00

4. Interpretation of the distribution and observed characteristics of exposed H_2O-rich areas

4.1 Spectral modeling

In a previous study, Combe et al. (2016) compared VIR spectra of the Oxo crater with laboratory spectra of mineral hydrates and H_2O ice, the latter providing the best fit. In all the cases, the shape of the 2.0 μm absorption band was the main spectral feature for the determination of the composition in H_2O ice, this absorption band is symmetric and centered at 2.0 μm, which is not the case for any of the mineral hydrates under consideration. Additional measurements performed by Singh et al. (2017, this issue) confirm that even mineral hydrates with higher solvation states (when a larger number of H_2O molecules are bonded to the mineral) than those initially used samples, and with sample temperatures more relevant to the surface of Ceres (180 K instead of 110K), do not exhibit H_2O absorption bands similar to those measured by VIR in the Oxo crater. In the present study, Fig. 4 and Fig. 5 show that in all nine H_2O-rich areas, the most diagnostic absorption band is always centered at 2.0 μm and symmetric, which provides straightforward spectral evidence that the H_2O-rich component is exposed H_2O ice. Most VIR spectra correspond to pixels that cover more than the H_2O-rich areas, because most of the nine sites are not spatially resolved. In the measured spectra by VIR, the large pixel footprint results in a contribution by H_2O-ice and a contribution by the surface materials around the H_2O-rich area, linearly combined (areal mixture). Combe et al. (2016) also determined that the VIR spectra of Oxo could be modeled by linear combinations of the average spectrum of Ceres with H_2O-ice spectrum.

In the present study, the H_2O-rich area associated with Oxo is spatially resolved by VIR. As a consequence, VIR spectra centered on this area exhibit the strongest H_2O absorption bands measured by VIR (42% in Fig. 15). Spectra of the Juling crater have also very strong H_2O absorption bands, which are presented in Raponi et al., (2017).

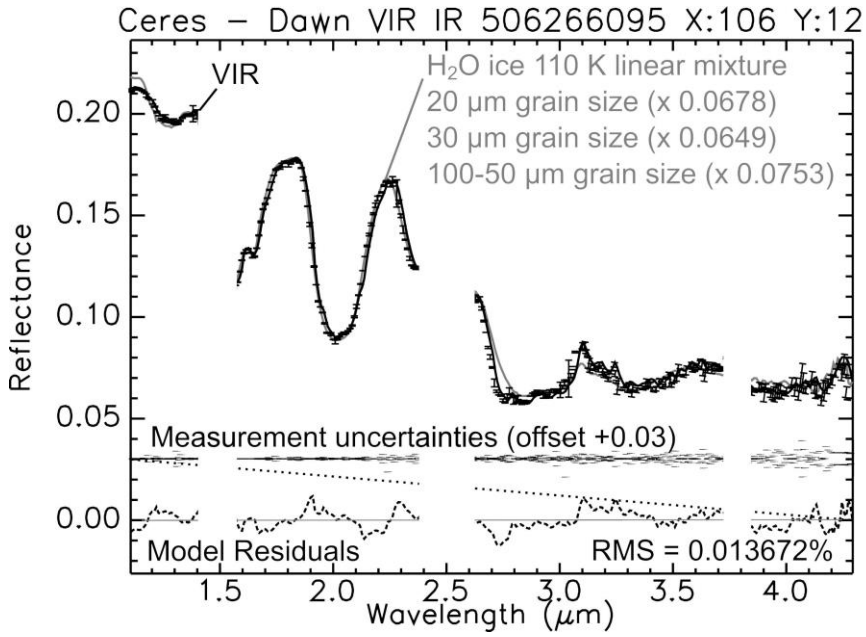

Fig. 15: VIR IR reflectance spectrum of Oxo acquired during LAMO modeled by a linear combination of three H_2O ice spectra (Hansen, 2009; Filacchione et al., 2016; Singh et al., 2017) with different grain size distributions and a low-albedo, spectrally neutral component (dotted line).

VIR spectra of Oxo provided the opportunity to perform further modeling. Raponi et al. (2016) obtained adequate spectral modeling results based on the radiative transfer theory of intimate mixing, using H_2O ice and various phyllosilicates found on Ceres.

Fig. 15 illustrates a test performed with pure H_2O ice. We used MELSUM (Combe et al., 2008) with different settings from those used in section 2.4. Here, we selected laboratory spectra of H_2O-ice samples with different grain size distribution as spectral endmembers. The temperature of the H_2O-ice samples that provide the reference spectra is 110 K. We used a computed straight line to account for high incidence angle, or low-albedo, spectrally neutral materials, and possible effects of Ceres' surface photometry that may affect the spectral slope. MELSUM automatically selected three reference spectra (combining three different grain sizes) to calculate the modeled spectrum that best fits the VIR spectrum. The result show that the shape of all H_2O-ice spectral features, such as the absorption bands at 1.28, 1.65 and 2.0 μm, and the Fresnel peak at 3.1 μm are also modeled accurately by a linear combination of H_2O-ice spectra. Model residuals have some anomalies, the amplitude of which is of the same order than measurement uncertainties (error bars) between 3.0 and 4.3 μm, and larger than measurement uncertainties between 1.1 and 3.0 μm. Uncertainties associated with the model are likely due in first order to the temperature in the simulated spectra of H_2O ice (110 K), which is lower than Ceres surface temperature by several tens of K. In particular, the shape of the H_2O absorption bands is sensitive to temperature variations (e.g. Hansen 2009). The limited distribution of grain sizes may also be a factor in the model, since the depth and width of an absorption band tend to increase with increasing grain size. In spite of the assumptions in the model and the observed anomalies in the residuals, the presence of spectral features associated with crystalline H_2O ice (the absorption bands and the Fresnel peak), both in the VIR spectrum and in the model have some significance. This modeling is supported by previous investigations which found that the H_2O-rich component on Ceres is crystalline H_2O ice (Combe et al., 2016; Raponi et al., 2017; Singh et al., this issue). Additional contributions by other surface components in VIR spectra may exist when the size of VIR pixels does not spatially resolve the H_2O-rich area. The H_2O ice may also be mixed with a spectral component similar to the average surface of Ceres, which is spectrally neutral in the range of wavelengths of the H_2O absorption bands. These results as well as those obtained by Raponi et al. (2016) indicate the non-uniqueness of the models, because similar quality of fit is obtained by selecting 20-100 μm grain sizes in linear combination of spectra, or by using larger grain sizes (100-200 μm) for H_2O ice and adding mineral components using the radiative transfer theory.

4.2 Distribution of H_2O-rich areas

There are two main characteristics that define the nine H_2O-rich areas detected by VIR: 1) The latitude is always above 30° (in both hemispheres); and 2) the area is limited to a few km^2 (6.8 at maximum in Oxo, which comprises three distinct areas), and most often on the order of 1 km^2. The maximum latitude of H_2O detection is only limited by the absence of coverage of the polar regions by VIR and by large incidence angles that create large areas of casted shadows where no observation is possible.

4.2.1 Comparison between VIR observations and other evidences of H_2O-rich materials

The latitude range is an indication of the role of illumination and surface temperature in the stability of the H_2O-rich component. The sublimation rate of H_2O ice, which varies by several orders of magnitude across all latitudes and throughout a complete revolution of Ceres around the sun (Landis et al., 2017), may explain the trend observed in the distribution of exposed H_2O ice. The temperature of the surface, illuminated or shadowed, depends on latitude, as does the depth to the

ice. The existence of H_2O ice above 30° latitude implies a recent exposure or a form of replenishment process, either endogenous (associated with areas of weak zones, or by mechanical exposure such as landslides or seismic shaking from nearby impacts), or surficial (such as the migration of H_2O molecules into cold traps), or external (such as meteorite impacts). This location is also where the sublimation rate, especially in poleward facing slopes, becomes very small.

In certain cases, such as the area at (44.61°N, 32.50°E in Fig. 14), the H_2O-rich material is exposed on surfaces that do not show any remarkable topographic features (not on a pole-facing slope, for example), and thus does not appear to be a cold trap. For that particular location, the aspect of the surface topography and morphology rules out the association with any impact, and thus with any form of external replenishment of H_2O. All the other small, high-albedo H_2O-rich areas are associated with small impact craters, however, the geological context and topography of these sites do not indicate any remarkable characteristics that could explain the existence of a cold trap. In absence of any other evidence, the most robust hypothesis is that a certain amount of H_2O ice present in the subsurface became exposed.

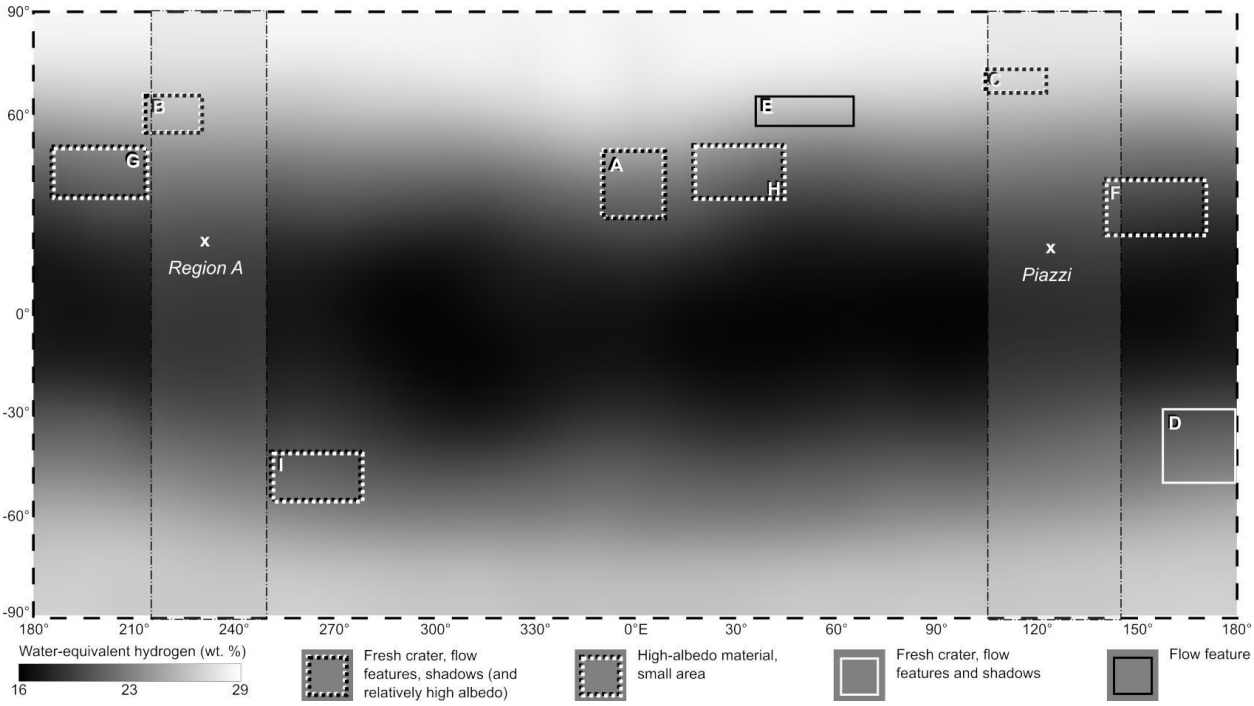

Fig. 16: Global distribution of water-equivalent hydrogen in the crust of Ceres from GRaND measurements (Prettyman et al., 2016) annotated with location of exposed H_2O-rich areas detected by VIR. The rectangles indicate the boundaries of FC context images, similar to Fig. 2, and the line style refer to the type of surface feature that is observed. The grey vertical bands and locations marked by an X labeled Region A and Piazzi refer to the two areas identified as possible sources of H_2O vapor outgassing by Küppers et al. (2014). Projection: Simple Cylindrical; central meridian: 0.

The four fresh impact craters (three in the northern hemisphere and Juling) that show flow features on the wall and floor likely favored the occurrences of landslides in an H_2O-rich terrain, which could expose that material. In the hypothesis that H_2O-ice is the main component, the sharp topography that casts shadows on their pole-facing slope likely slows down the sublimation rate, which in turns increases the probability of detection over periods of several months, as was done by Dawn's instruments.

The global distribution of H_2O-equivalent hydrogen from GRaND measurements (Fig. 16) shows minimum values along the equator and maximum values near the poles. All detections of exposed H_2O ice by VIR occur where the average regional abundance of H_2O-equivalent hydrogen is above 20 wt. %. The depth-to-ice on Ceres depends on latitude, as temperatures vary between the poles and the equator. In the polar regions, the regolith appears ice-free in images and reflectance spectra, although GRaND does detect H in abundance near the surface. These observations are consistent with models of ice retreat that suggest that the ice-free topmost layer may be less than a centimeter thick (Schorghofer, 2016). At the equator, the expected depth to the ice table depends on the physical properties of the lag (Fanale & Salvail 1989), but could be less than a meter (Prettyman et al., 2016). Such a thin overburden layer makes it plausible that ice can be exposed by minor mechanical disturbances, such as impacts and landslides.

The overlying ice-free layer has two functions for the preservation of subsurface ice. First, it represents a diffusive barrier that water molecules must traverse, and second, it attenuates the temperature amplitude, such that the peak temperatures felt by the buried ice are less than those on the very surface. This causes a significant difference between the sublimation rate of exposed ice (Landis et al., 2017) and that of buried ice. It explains why exposed ice is currently rare on Ceres, despite the claim of ubiquitous presence of H_2O ice in the subsurface (e.g., Prettyman et al., 2016; Castillo-Rogez et al., in revision).

4.2.2 Comparison between Dawn/VIR and Herschel observations

H_2O at the surface of Ceres was inferred from the interpretation of H_2O outgassing that was revealed by spectra from the Herschel telescope Küppers et al. (2014). No detection of H_2O has been made by Dawn on the two sites identified as Piazzi and Region A in Herschel observations (Fig. 2 and Fig. 16). However, since other H_2O-rich objects in the Main Asteroid Belt are observed by telescope but not by Dawn, such as (24) Themis (Campins et al., 2010) and (65) Cybele (Licandro et al., 2011), Ceres offers the opportunity to make a comparison.

The latitude range of H_2O-rich areas identified by VIR (> 30°, North and South) is in contradiction with the values of 21°N and 23°N that resulted from modeling presented in Herschel observations. With VIR, the precision of the location is determined by the spatial resolution of the instrument. With Herschel, the latitude of H_2O outgassing reported in Küppers et al. (2014) was determined based on a model that is used to fit the observations. The uniqueness of this model is not well documented, and therefore there may be more than one latitude that could explain the observation for each site.

Within the two ranges of longitudes where H_2O outgassing was interpreted from Herschel observations (110°-145°E and 215°-250°E), exposed H_2O ice is detected by VIR, which might indicate a relationship between the two types of observation. However the large longitudes ranges (35°) provided by Küppers et al. (2014) must be compared with the number (ten) of H_2O-rich sites detected by VIR globally (over 360° in longitude), which corresponds to an average longitude spacing of 36°. In VIR data, the two largest longitude ranges between two H_2O-rich areas are 95° and 60° respectively. As a result, assuming a random location of the 35°-large bands over Ceres, there is ~80% probability that one longitude range contains at least one local area of exposed H_2O ice detected by VIR, and ~70% probability that the two longitude ranges contain at least one H_2O-rich area observed by VIR.. According to these numbers, the apparent agreement between the two observations is inconclusive: to date, it is not possible to relate the H_2O-rich areas observed by VIR with the H_2O outgassing regions reported by Küppers et al. (2014).

Finally, the total area of exposed H_2O ice by VIR is in the range of 10-20 km^2, whereas the outgassing surface calculated from Herschel observations is 0.6 km^2. The difference in estimated area may be only an apparent discrepancy, because the two values correspond to different

characteristics of the surface. Comparing the two numbers would imply that the entire area of exposed H_2O ice observed by VIR should be outgassing. In addition, the solar illumination – and thus the surface temperature – of any given H_2O-rich area varies throughout a cerean day due to the local topography, which may trigger sporadic outgassing. Consequently, on average, the outgassing area at any given time may be smaller than 1 km^2, even if the total H_2O-rich area is larger by one order of magnitude.

5. Conclusions

Absorption bands at 2.0 μm (and 1.65 and 1.28 μm) have been detected in VIR spectra at 9 different locations on Ceres, implying exposed H_2O-rich materials at the surface. Modeling of VIR spectra (e.g. Combe et al., 2016; Raponi et al., 2016) indicates H_2O ice as the component that most likely explains the H_2O detections in the spectra.

Each detection of H_2O absorption bands in the VIR spectra is associated with one or more distinctive surface features, such as a surface material with higher albedo than its surrounding terrains, or nearby a flow-like morphological feature observed at high resolution FC images. Three H_2O-rich areas have all these characteristics together, while the other six do not. Four of these sites are associated with persistent shadows. On the other hand, the observation of one or more distinctive surface features (high albedo, or flow-like feature, or persistent shadow) does not imply the detection of H_2O absorption bands in VIR spectra.

The spectral modeling of VIR spectra of H_2O-rich areas provides the best fit with H_2O ice, regardless of the technique used (intimate mixing by Raponi et al. (2016) based on the radiative transfer theory and the use of optical constants, or linear spectral unmixing of laboratory spectra or modeled spectra combining different distributions of grain sizes presented in this study).

All H_2O absorption features are detected at latitudes above 30°, and correspond to areas of a few km^2 at maximum (three H_2O-rich areas associated with the Oxo crater cover a total of 6.8 km^2, and the northern wall of the Juling crater alone may represent about 6 km^2). This distribution is consistent with temperature-dependent stability, which is expected for H_2O ice. Since H_2O ice in sunlit areas is short-lived on Ceres (Hayne & Aharonson, 2015; Formisano et al., 2016; Titus, 2015) at low latitude, these observations suggest that H_2O is present in the subsurface, the spectral detections imply that it has been recently exposed on the surface.

VIR detections of exposed H_2O at the surface of Ceres provide compeling evidence that H_2O ice is present in abundance in the subsurface, as originally suggested by low bulk density and modeling (McCord and Sotin, 2005), and now inferred from Dawn's observations of morphological flow-like features (Schmidt et al., 2017), interpretations of past cryovolcanism at Ahuna Mons (Ruesch et al., 2016; Nathues et al., 2017), the detection of excess elemental hydrogen in the crust (Prettyman et al., 2016), and models of the internal structure of Ceres from gravity and shape measurements (Park et al., 2016).

On Ceres, subsurface ice is ubiquitous (Prettyman et al., 2016), whereas exposed ice is rare. This finding has important implications for searching ice-rich small celestial bodies with Earth-based telescopes. As viewed from Earth or Earth-orbit, ice on the surface of main belt asteroids is rare, and even the Jovian Trojans appear to be mostly free of surface ice (Yang & Jewitt, 2007). Ceres is an example of an ice-rich body for which no detection of surface ice has been possible yet from Earth.

Acknowledgments

686 The funding for this research was provided under the NASA Dawn mission through a
687 subcontract (2090-S-MB516) from the University of California, Los Angeles. The VIR instrument
688 and VIR team are funded by ASI (Italian Space Agency) and INAF (Istituto Nazionale di
689 Astrofisica).

References

A'Hearn M. F., Feldman P. D., 1992, Water vaporization on Ceres. *Icarus* 98, 54-60.

Acton C. H., 1996, Ancillary data services of NASA's Navigation and Ancillary Information Facility, Planetary and Space Science, Volume 44, Issue 1, p. 65-70, doi: 10.1016/0032-0633(95)00107-7.

Akimov L. A., 1975, Influence of mesorelief on the brightness distribution over a planetary disk, Astronomicheskii Zhurnal, vol. 52, May-June 1975, p. 635-641. Soviet Astronomy, vol. 19, no. 3, 1976, p. 385-388. Translation.

Ammannito E. et al., 2016, The Distribution of Phyllosilicates on Ceres, Science 353.

Campins H.; Hargrove K; Pinilla-Alonso N; Howel, E. S.; Kelley M. S.; Licandro J; Mothé-Diniz T; Fernández Y; Ziffer J, 2010, Water ice and organics on the surface of the asteroid 24 Themis, Nature. 464, 1320–1321, doi: 10.1038/nature09029.

Carrozzo F. G. Raponi A., Sanctis M. C., Raponi A., Ammannito E., Giardino M., D'Aversa E, Fonte S., Tosi F., Capaccioni F., Capria M. T., Ciarniello M., Longobardo A., Palomba E., Zambon F., Russell C. T., Raymond C. A., 2016, Artefacts removal in VIR/DAWN data, Rev. Sci. Instrum. 87, 124501, DOI: http://dx.doi.org/10.1063/1.4972256.

Castillo-Rogez J., McCord T. B., 2010, Ceres' evolution and present state constrained by shape data. Icarus 205, 443-459.

Combe J.-Ph., McCord T. B., Tosi F., Ammannito E., Carrozzo F. G., De Sanctis M. C., Raponi A., Byrne S., Landis M., Hughson K. H. G., Raymond C. A., Russell C. T., 2016, Detection of local H_2O exposed at the surface of Ceres, Science, Volume 353, Issue 6303, doi: 10.1126/science.aaf3010.

Combe J.-Ph. et al., 2015, Reflectance properties and hydrated material distribution on Vesta: Global investigation of variations and their relationship using improved calibration of Dawn VIR mapping spectrometer. Icarus 259, 21-38.

Combe J.-Ph. et al., 2008, Analysis of OMEGA/Mars Express data hyperspectral data using a Multiple-Endmember Linear Spectral Unmixing Model (MELSUM): Methodology and first results. Planet Space Sci. 56, 951-975.

Combe et al., 2017, Surface composition of Ezinu quadrangle on Ceres, Icarus, this issue, in preparation.

De Sanctis M. C. et al., 2011, The VIR Spectrometer. Space Science Rev. 163, 329-369.

De Sanctis M. C., Ammannito E., Raponi A., Marchi S., McCord T. B., McSween H. Y. Capaccioni F. Capria M. T. Carrozzo F. G., Ciarniello M., Longobardo A., Tosi F., Fonte S., Formisano M., Frigeri A., Giardino M., Magni G., Palomba E., Turrini D., Zambon F., Combe J.-P., Feldman, W., Jaumann R., McFadden L. A., Pieters C. M., Prettyman T., Toplis, M., Raymond C. A., Russell C. T., 2015, Ammoniated phyllosilicates with a likely outer Solar System origin on (1) Ceres, Nature, Volume 528, Issue 7581, pp. 241-244, 10.1038/nature16172.

De Sanctis M. C., Raponi A., Ammannito E., Ciarniello M., Toplis M. J., McSween H. Y., Castillo-Rogez J. C., Ehlmann B. L., Carrozzo F. G., Marchi S., Tosi F., Zambon F., Capaccioni F., Capria M. T., Fonte S., Formisano M., Frigeri A., Giardino M., Longobardo A., Magni G.,

731 Palomba E., McFadden L. A., Pieters C. M., Jaumann R., Schenk P., Mugnuolo R., Raymond
732 C. A., Russell C. T., 2016, Bright carbonate deposits as evidence of aqueous alteration on (1)
733 Ceres, Nature, Volume 536, Issue 7614, pp. 54-57, doi: 10.1038/nature18290.

734 Ermakov, A. I., E. Mazarico, S. E. Schroder, U. Carsenty, N. Schorghofer, F. Preusker, C.A.
735 Raymond, C. T. Russell, M. T. Zuber, 2017. Ceres obliquity history and implications for the
736 permanently shadowed regions. Geophysical Research Letters 44, 2652-2661, doi:
737 10.1002/2016GL072250.

738 Fanale F. P. and Salvail J. R., 1989, The water regime of asteroid (1) Ceres, Icarus (ISSN 0019-1035),
739 vol. 82, Nov. 1989, p. 97-110, doi: 10.1016/0019-1035(89)90026-2.

740 Filacchione, G.; de Sanctis, M. C.; Capaccioni, F.; Raponi, A.; Tosi, F.; Ciarniello, M.; Cerroni, P.;
741 Piccioni, G.; Capria, M. T.; Palomba, E.; Bellucci, G.; Erard, S.; Bockelee-Morvan, D.;
742 Leyrat, C.; Arnold, G.; Barucci, M. A.; Fulchignoni, M.; Schmitt, B.; Quirico, E.; Jaumann,
743 R.; Stephan, K.; Longobardo, A.; Mennella, V.; Migliorini, A.; Ammannito, E.; Benkhoff, J.;
744 Bibring, J. P.; Blanco, A.; Blecka, M. I.; Carlson, R.; Carsenty, U.; Colangeli, L.; Combes, M.;
745 Combi, M.; Crovisier, J.; Drossart, P.; Encrenaz, T.; Federico, C.; Fink, U.; Fonti, S.; Ip, W.
746 H.; Irwin, P.; Kuehrt, E.; Langevin, Y.; Magni, G.; McCord, T.; Moroz, L.; Mottola, S.;
747 Orofino, V.; Schade, U.; Taylor, F.; Tiphene, D.; Tozzi, G. P.; Beck, P.; Biver, N.; Bonal, L.;
748 Combe, J.-Ph.; Despan, D.; Flamini, E.; Formisano, M.; Fornasier, S.; Frigeri, A.; Grassi, D.;
749 Gudipati, M. S.; Kappel, D.; Mancarella, F.; Markus, K.; Merlin, F.; Orosei, R.; Rinaldi, G.;
750 Cartacci, M.; Cicchetti, A.; Giuppi, S.; Hello, Y.; Henry, F.; Jacquinod, S.; Reess, J. M.;
751 Noschese, R.; Politi, R.; Peter, G., 2016, Exposed water ice on the nucleus of comet
752 67P/Churyumov-Gerasimenko, Nature, Volume 529, Issue 7586, pp. 368-372, doi:
753 10.1038/nature16190.

754 Formisano M., De Sanctis M. C., Magni G., Federico C. & Capria M. T., 2016, Ceres water regime:
755 surface temperature, water sublimation and transient exo(atmo)sphere, *Monthly Notices of the*
756 *Royal Astron. Soc. 455*, 1892-1904.

757 Hayne P. O. & Aharonson O., 2015, Thermal stability of ice on Ceres with rough topography, J.
758 Geophys. Res. 120, 1567-1584.

759 Hansen G. B, 2009, Calculation of single-scattering albedos: Comparison of Mie results with Hapke
760 approximations, Icarus, Volume 203, Issue 2, p. 672-676, doi: 10.1016/j.icarus.2009.05.025

761 Jewitt D., 1996, From comets to asteroids: When hairy stars go bald. *Earth, Moon, and Planets*, 72,
762 185-201.

763 Küppers M. et al., 2014, Localized sources of water vapour on the dwarf planet (1) Ceres. Nature
764 505 (7484), 525-527.

765 Landis, M. E.; Byrne, S.; Schörghofer, N.; Schmidt, B. E.; Hayne, P. O.; Castillo-Rogez, J.; Sykes, M.
766 V.; Combe, J.-P.; Ermakov, A. I.; Prettyman, T. H.; Raymond, C. A.; Russell, C. T., 2017,
767 Conditions for Sublimating Water Ice to Supply Ceres' Exosphere, Journal of Geophysical
768 Research: Planets, 122 (10), 1984-1995, doi: 10.1002/2017JE005335

769 Lebofsky L. A., Feierberg M. A., Tokunaga A. T., Larson H. P., Johnson J. R., 1981, The 1.7- to 4.2-
770 micron spectrum of asteroid 1 Ceres - Evidence for structural water in clay minerals. *Icarus*
771 48**,** 453-459.

772 Licandro J.; Campins H.; Kelley M.; Hargrove K.; Pinilla-Alonso N.; Cruikshank D.; Rivkin A. S.;
773 Emery J., 2011, (65) Cybele: detection of small silicate grains, water-ice, and organics,
774 Astronomy and Astrophysics, 525, doi: 10.1051/0004-6361/201015339.

775 Li J.-Y.; Reddy V.; Nathues A.; Le Corre L.; Izawa M. R. M.; Cloutis E. A.; Sykes M. V.; Carsenty U.;
776 Castillo-Rogez J. C.; Hoffmann M.; Jaumann R.; Krohn K.; Mottola S.; Prettyman T. H.;
777 Schaefer M.; Schenk P.; Schröder S. E.; Williams D. A.; Smith D. E.; Zuber M. T.; Konopliv
778 A. S.; Park R. S.; Raymond . A.; Russell C. T., 2016, The Astrophysical Journal Letters,
779 Volume 817, Issue 2, article id. L22, 7 pp., doi: 10.3847/2041-8205/817/2/L22.

780 Longobardo, A.; Palomba, E.; De Sanctis, M. C.; Ciarniello, M.; Tosi, F.; Carrozzo, F. G.; Raponi,
781 A.; Zambon, F.; Ammannito, E.; Li, J.-Y.; Raymond, C. A.; Russell, C. T., 2016, Average
782 Photometric Properties of Ceres Spectral Parameters, 47th Lunar and Planetary Science
783 Conference, held March 21-25, 2016 at The Woodlands, Texas. LPI Contribution No. 1903,
784 p.2239.

785 McCord T. B., Sotin C., 2005, Ceres: Evolution and current state. J. Geophys. Res. 110.

786 Milliken R. E., Rivkin A. S., **2009,** Brucite and carbonate assemblages from altered olivine-rich
787 materials on Ceres. *Nat. Geosci.* 2, 258–261.

788 Nathues A. et al., 2015, Sublimation in bright spots on (1) Ceres. Nature 528, 237-240.

789 Nathues, A.; Hoffmann, M.; Schaefer, M.; Le Corre, L.; Reddy, V.; Platz, T.; Cloutis, E. A.;
790 Christensen, U.; Kneissl, T.; Li, J.-Y.; Mengel, K.; Schmedemann, N.; Schaefer, T.; Russell,
791 C. T.; Applin, D. M.; Buczkowski, D. L.; Izawa, M. R. M.; Keller, H. U.; O'Brien, D. P.;
792 Pieters, C. M.; Raymond, C. A.; Ripken, J.; Schenk, P. M.; Schmidt, B. E.; Sierks, H.; Sykes,
793 M. V.; Thangjam, G. S.; Vincent, J.-B., 2015, Sublimation in bright spots on (1) Ceres,
794 Nature, Volume 528, Issue 7581, pp. 237-240, doi: 10.1038/nature15754.

795 Nathues, A.; Hoffmann, M.; Platz, T.; Thangjam, G. S.; Cloutis, E. A.; Reddy, V.; Le Corre, L.; Li, J.-
796 Y.; Mengel, K.; Rivkin, A.; Applin, D. M.; Schaefer, M.; Christensen, U.; Sierks, H.; Ripken,
797 J.; Schmidt, B. E.; Hiesinger, H.; Sykes, M. V.; Sizemore, H. G.; Preusker, F.; Russell, C. T.
798 2016, FC colour images of dwarf planet Ceres reveal a complicated geological history,
799 Planetary and Space Science, 134, 122-127, doi: 10.1016/j.pss.2016.10.017.

800 Nathues, A.; Platz, T.; Hoffmann, M.; Thangjam, G.; Cloutis, E. A.; Applin, D. M.; Le Corre, L.;
801 Reddy, V.; Mengel, K.; Protopapa, S.; Takir, D.; Preusker, F.; Schmidt, B. E.; Russell, C. T.,
802 2017, Oxo Crater on (1) Ceres: Geological History and the Role of Water-ice, The
803 Astronomical Journal, 154,doi: 10.3847/1538-3881/aa7a04.

804 Park, R. S.; Konopliv, A. S.; Bills, B. G.; Rambaux, N.; Castillo-Rogez, J. C.; Raymond, C. A.;
805 Vaughan, A. T.; Ermakov, A. I.; Zuber, M. T.; Fu, R. R.; Toplis, M. J.; Russell, C. T.;
806 Nathues, A.; Preusker, F., A partially differentiated interior for (1) Ceres deduced from its
807 gravity field and shape, Nature, Volume 537, Issue 7621, pp. 515-517, doi:
808 10.1038/nature18955.

809 Platz T., Nathues A., Schorghofer N., Preusker F., Mazarico E., Schröder S. E., Byrne S., Kneissl T.,
810 Schmedemann N., Combe J.-P., Schäfer M., Thangjam G. S., Hoffmann M., Gutierrez-
811 Marques P., Landis M. E., Dietrich W., Ripken J., Matz K.-D. & Russell C. T., 2016, Surface
812 water-ice deposits in the northern shadowed regions of Ceres, Nature Astronomy,
813 doi:10.1038/s41550-016-0007.

814 Pieters C. M., 1983, Strength of mineral absorption features in the transmitted component of near-
815 infrared reflected light - First results from RELAB, Journal of Geophysical Research (ISSN
816 0148-0227), vol. 88, Nov. 10, 1983, p. 9534-9544, doi: 10.1029/JB088iB11p09534

817 Prettyman, T. H.; Yamashita, N.; Castillo-Rogez, J. C.; Feldman, W. C.; Lawrence, D. J.; McSween,
818 H. Y.; Schorghofer, N.; Toplis, M. J.; Forni, O.; Joy, S. P.; Marchi, S.; Platz, T.; Polanskey, C.
819 A.; De Sanctis, M. C.; Rayman, M. D.; Raymond, C. A.; Russell, C. T., 2016, Extensive water
820 ice within Ceres' aqueously altered regolith: Evidence from nuclear spectroscopy. *Science 355,*
821 55-59, doi 10.1126/science.aah6765.

822 Raponi, A.; Ciarniello, M.; De Sanctis, M. C.; Ammannito, E.; Capaccioni, F.; Capria, M. T.;
823 Carrozzo, F. G.; Frigeri, A.; Fonte, S.; Giardino, M.; Longobardo, A.; Magni, G.; Palomba,
824 E.; Tosi, F.; Zambon, F.; Raymond, C. A.; Russell, C. T., 2016, Ceres spectral modelling with
825 VIR data onboard Dawn: Method and first results, European Planetary Science Congress
826 2015, held 27 September - 2 October, 2015 in Nantes, France

827 Raponi et al., 2017, in preparation

828 Rivkin A. S., Volquardsen E. L., Clark B. E., 2006, The surface composition of Ceres: Discovery of
829 carbonates and iron-rich clays. *Icarus* 185, 563–567.

830 Roatsch Th. et al., 2016, Ceres Survey Atlas derived from Dawn Framing Camera images. Planet.
831 Space Sci. 121, 115–120.

832 Ruesch O. et al., 2016, Cryovolcanism on Ceres, *Science* 353.

833 Schmidt B. E.; Hughson K. H. G.; Chilton H. T.; Scully J. E. C.; Platz T.; Nathues A.; Sizemore H.;
834 Bland M. T.; Byrne S.; Marchi S.; O'Brien D. P.; Schorghofer N.; Hiesinger H.; Jaumann R.;
835 Pasckert J. H.; Lawrence J. D.; Buzckowski D.; Castillo-Rogez J.; Sykes M. V.; Schenk P. M.;
836 De Sanctis M. C.; Mitri G.; Formisano M.; Li J.-Y.; Reddy V.; Le Corre L.; Russell C. T.;
837 Raymond C. A., 2017, Geomorphological evidence for ground ice on dwarf planet Ceres,
838 Nature Geoscience, 10 (5), 338-343, doi: 10.1038/ngeo2936.

839 Russell C. T., Raymond C. A., 2011, The Dawn Mission to Vesta and Ceres. Space Science Rev. 163,
840 3-23.

841 Schröder, S. E.; Mottola, S.; Carsenty, U.; Ciarniello, M.; Jaumann, R.; Li, J.-Y.; Longobardo, A.;
842 Palmer, E.; Pieters, C.; Preusker, F.; Raymond, C. A.; Russell, C. T., 2017, Resolved
843 Spectrophotometric Properties of the Ceres Surface from Dawn Framing Camera Images,
844 Astrophysics - Earth and Planetary Astrophysics, doi:10.1016/j.icarus.2017.01.026

845 Schorghofer, N.; Mazarico, E.; Platz, T.; Preusker, F.; Schröder, S. E.; Raymond, C. A.; Russell, C.
846 T., 2016, The permanently shadowed regions of dwarf planet Ceres. Geophysical Research
847 Letters 43, 6783-6789. doi:10.1002/2016GL069368.

848 Schorghofer, N. 2016, Predictions of depth-to-ice on asteroids based on an asynchronous model of
849 temperature, impact stirring, and ice loss. *Icarus* 276, 88-95.

850 Shkuratov, Yu. G.; Kreslavsky, M. A.; Ovcharenko, A. A.; Stankevich, D. G.; Zubko, E. S.; Pieters,
851 C.; Arnold, G., 1999, Opposition Effect from Clementine Data and Mechanisms of
852 Backscatter, Icarus, Volume 141, Issue 1, p. 132-155, doi: 10.1006/icar.1999.6154

853 Singh et al., 2017, Laboratory spectra of H_2O ice and mineral hydrates relevant to the Dawn mission
854 at Ceres, Icarus, this issue.

855 Thangjam, G.; Hoffmann, M.; Nathues, A.; Li, J.-Y.; Platz, T., 2016, Haze at Occator Crater on
856 Dwarf Planet Ceres, The Astrophysical Journal Letters, Volume 833, Issue 2, article id. L25,
857 9 pp, doi: 10.3847/2041-8213/833/2/L25.

858 Thomas P. C. et al., 2005, Differentiation of the asteroid Ceres as revealed by its shape. Nature 437,
859 224–226.

860 Titus T., 2015, Ceres: Predictions for near-surface water ice stability and implications for plume
861 generating processes, *Geophys. Res. Let. 42*, 2130-2136.

862 Vernazza P. *et al.*, 2005, Analysis of near-IR spectra of 1 Ceres and 4 Vesta, targets of the Dawn
863 mission. *Astron. & Astrophys.* 436, 1113-1121.

864 Villarreal, M. N.; Russell, C. T.; Luhmann, J. G.; Thompson, W. T.; Prettyman, T. H.; A'Hearn, M.
865 F.; Küppers, M.; O'Rourke, L.; Raymond, C. A., 2017, The dependence of the Cerean
866 exosphere on solar energetic particle events. The Astrophysical Journal Letters, 838, L8, doi:
867 10.3847/2041-8213/aa66cd.

868 Xu S., Binzel R. P., Burbine T. H., Bus S. J., 1995, Small main-belt asteroid spectroscopic survey:
869 Initial results, Icarus (ISSN 0019-1035), vol. 115, no. 1, p. 1-35, doi: 10.1006/icar.1995.1075.

870 Yang B., Jewitt D., 2007, Spectroscopic search for water ice on Jovian Trojan asteroids. The
871 Astronomical Journal 134(1), 223.

872
873